A moving-least-squares immersed boundary method for simulating the fluid–structure interaction of elastic bodies with arbitrary thickness

Original Citation:
A moving-least-squares immersed boundary method for simulating the fluid–structure interaction of elastic bodies with arbitrary thickness / DE TULLIO, Marco Donato; Pascazio, Giuseppe. - In: JOURNAL OF COMPUTATIONAL PHYSICS. - ISSN 0021-9991. - STAMPA. - 325:(2016), pp. 201-225. [10.1016/j.jcp.2016.08.020]

Published version
DOI:10.1016/j.jcp.2016.08.020

Publisher:

A Moving-Least-Squares Immersed Boundary Method for simulating the fluid-structure interaction of elastic bodies with arbitrary thickness

M. D. de Tullio*, G. Pascazio

Dipartimento di Meccanica, Matematica e Management, DMMM
Centro di Eccellenza in Meccanica Computazionale, CEMeC
Politecnico di Bari, Via Re David 200, 70125, Bari, Italy

Abstract

A versatile numerical method for the fluid-structure-interaction of bodies with arbitrary thickness, immersed in an incompressible fluid, is presented, with the aim of simulating different biological engineering applications. A discrete-forcing immersed boundary method is adopted, based on a moving least squares approach to reconstruct the solution in the vicinity of the immersed surface. A simple spring-network model is considered for describing the dynamics of deformable structures, in order to have the freedom of easily model and simulate different biological systems that can not always be described by simple continuum models, without affecting the computational time and simplicity of the overall method. The fluid and structures are coupled in a strong way, in order to avoid instabilities related to large accelerations of the bodies. The method gives accurate results comparable with that of sharp direct-forcing approach, and can manage pressure differences across the surface in one grid cell, still obtaining very smooth forces. The effectiveness of the method has been validated by means of several test cases involving: rigid bodies, either falling in a quiescent fluid, fluttering or tumbling, or transported by a shear flow; infinitely thin elastic structures with mass, such as a two-dimensional flexible filament and an inverted flexible filament in a free stream; a three-dimensional model of a bio-prosthetic aortic valve opening and closing under a pulsatile flowrate. A very good agreement is obtained in all cases, comparing with available experimental

---

*Corresponding author. E-mail address: marcodonato.detullio@poliba.it

Preprint submitted to J. Comput. Phys. *March 9, 2021*

data and numerical results obtained by different methods.

Keywords: Immersed Boundary Method, Fluid-Structure Interaction, Network Spring Model, Direct Forcing with Moving Least Squares, Elastic Zero-thickness Body, Flexible Filament

---

1. Introduction

Fluid-structure interaction (FSI) problems are found in many engineering areas. The three-dimensional computational modeling is particularly challenging and has recently encountered the interest of several research groups. Among different FSI problems, biological applications are becoming of ever increasing interest in the scientific community and their accurate and efficient numerical simulation provides an essential means in understanding the fundamental physics and reducing the time needed for experiments. The accurate description of FSI can not ignore the fact that moving and/or deforming bodies act on the surrounding fluid that is forced to move accordingly (no-slip condition), and reacts with pressure and velocity gradients distribution that, in turn, produces the surface forces that cause the motion of the body. This poses several challenges for the numerical approaches adopted. With no intent of being exhaustive, one can mention: rigid particle of arbitrarily shape transported by the fluid; deformable particles in shear flows (capsules, vesicles, cells), constituted by a liquid droplet enclosed by a structure with thickness much smaller than the particle size; elastic slender bodies immersed in a fluid, such as flags, insect wings, jellyfishes, bioprosthetic heart valves, where a thin surface is significantly deformed by the fluid. In the mentioned cases, describing the dynamics of the interaction between the body and the fluid is not a trivial task, since the numerical method needs to be able to handle in an efficient way complex and very thin geometries undergoing large deformations, without loosing accuracy.

Given the large displacements/deformations of the bodies, body-fitted approaches [1, 2], both structured and unstructured, are not the optimal choice. They need the time-consuming regeneration or deformation of the mesh and the successive projection of the flow field solution from previous mesh to new one, which can lead to a decrease of accuracy. Immersed Boundary (IB) methods [3, 4] are more suitable, since the governing equations are solved on a fixed grid, covering the whole domain, thus including points that rely inside the closed boundaries (if any). Continuous forcing IB methods derived by the classical approach proposed by Peskin [3] have been widely used, considering different biological and engineering applications involving elastic slender bodies [5, 6, 7, 8]. An advantage of these monolithic approaches is the inherent strong coupling for fluid-structure-interaction and their simplicity. On the other hand, they have a fundamental difficulty in handling structures with mass and the immersed interface is smeared by distributing the forcing terms over several grid nodes in the vicinity of the solid boundary. An alternative is to consider partitioned algorithms, in which the fluid and structures are solved independently and then coupled, as done in [9] for studying flexible filaments, adopting a feedback forcing approach[10], but with a severe limitation on the numerical integration time-step. On the other hand, direct forcing methods [11] are particularly attractive, for their moderate limitation of the computational time step [12, 4]. They give very good results for fixed boundaries, but their extension to FSI problems needs particular attention in order to attenuate spurious oscillation of hydrodynamic forces that are potential source of instabilities [13, 14, 15, 16, 17]. The alternative direct-forcing scheme of Uhlmann [13], computing the forcing term on Lagrangian markers (laying on the immersed body), provides smooth hydrodynamic forces, with the requirement of a uniform distribution of the markers on the body. Vanella and Balaras [15] improved Uhlmann's approach [13], by using a versatile moving-least-squares (MLS) approximation to build the transfer functions between the Eulerian and Lagrangian grids for rigid bodies. Discrete-forcing IB method have been used for studying deformable bodies [18, 19, 20, 21, 22] with good accuracy.

The aim of this work is to build a numerical tool for simulating the fluid-structure-interaction of arbitrarily shaped, very thin surfaces, both rigid and deformable, so as to be able to describe the dynamics of either closed (enclosing a volume) particles, both solid and deformable, such as capsules or biological cells [23, 24], or open, describing zero-thickness slender bodies. In order to achieve such a goal, several ingredients are coupled together forming an accurate, efficient and simple code. A partitioned, discrete-forcing IB method is adopted, based on a MLS approach, similar to [15], in order to reconstruct the solution in the vicinity of the immersed surface and to convert the Lagrangian forcing back to the Eulerian grid for the case of thin surfaces that can be rigid or undergo large deformations. With the aim of describing different biological systems that may consist of diversely scaled elements (e.g. cells, organ tissues) and that can not always be described by simple continuum models, for the case of non rigid bodies we adopted a simple but very versatile methodology based on spring-network models. The surface is discretized by a triangulated mesh and the mass is assumed to be distributed on the nodes of the triangles; these are connected by in-plane and out-of-plane (bending) springs in order to model the structural elastic behavior [25]. For both rigid and deformable bodies, the fluid and structures are coupled in a strong way, in order to avoid instabilities related to strong accelerations of the mass-points. A 4-th order predictor-corrector method is adopted, based on Hamming's method with mop-up correction [26]. Particular attention is required in determining the hydrodynamic loading on the structure, considering the thinness of the bodies. The method gives accurate results comparable with that of sharp direct-forcing approach, and can manage pressure differences across the surface in one grid cell. Moreover, the method is able to obtain very smooth forces, needed by the FSI approach. The only restriction to the computational time step is related to the flow solver stability condition and to the accuracy needed in determining the body dynamics, depending on the specific problem under study. The tool has been validated by means of several test cases of increasing complexity, involving closed surfaces, enclosing a volume, and rigid particles: the sedimentation of an elliptic particle in a quiescent fluid, the fluttering and tumbling dynamics of a falling plate and a single sphere settling under gravity, as well as a circular particle transport in a planar Couette flow are considered. On the other hand, open surfaces representing infinitely thin elastic structures with mass are considered: a two-dimensional flexible filament and an inverted flexible filament in a free stream. Finally, a three-dimensional model of a bio-prosthetic aortic valve is considered, with nonlinear and anisotropic mechanical properties, opening and closing during the pulsatile cardiac cycle. A good agreement has been obtained in the cases where numerical and/or experimental results are available in the literature, considering both the rigid motion as well as the deformation dynamics.

It is important to note that the procedure is very general, and both fluid and structure solvers can be replaced by more suitable ones, depending on the problem of interest. A straightforward extension is the use of a finite-element structural solver for describing the dynamics of deformable slender surfaces (e.g. membrane solver of [27]) maintaining the same data structure and formalism, with just an increase of the computational cost due to the structural solver. Moreover, the presented methodology has been adopted on non-uniform structured Cartesian grids, but it can be easily extended to unstructured meshes, provided that the minimum number of Eulerian grid points in the support domain, needed by the MLS procedure is provided.

2. Numerical method

2.1. Flow solver

Under the assumption of incompressible flow, the governing equations for the fluid dynamics are the Navier–Stokes and continuity equations:

$$\rho_f \left(\frac{\partial \boldsymbol{u}}{\partial t} + \boldsymbol{u} \cdot \nabla \boldsymbol{u} \right) = -\nabla p + \mu \nabla^2 \boldsymbol{u} + \rho_f \boldsymbol{f} \tag{1}$$

$$\boldsymbol{\nabla} \cdot \boldsymbol{u} = 0 \tag{2}$$

where ρ_f is the fluid density, $\boldsymbol{u}$ is the fluid velocity, p is the pressure, μ is the fluid dynamic viscosity and $\boldsymbol{f}$ contains the forcing terms, such as that of the IB technique. The above equations are non-dimensionalized, introducing the Reynolds number $Re = \frac{\rho_f U L}{\mu}$, with U and L a reference velocity and length, respectively. The non-linear terms are discretized by an explicit Adams–Bashforth scheme and the linear viscous terms by an implicit Crank–Nicolson scheme, yielding the following semi-discrete equation:

$$\frac{\hat{\boldsymbol{u}} - \boldsymbol{u}^n}{\Delta t} = -\alpha \boldsymbol{\nabla} p^n + \gamma\, H^n + \rho\, H^{n-1} + \frac{\alpha}{2\, Re} \nabla^2 \left(\hat{\boldsymbol{u}} + \boldsymbol{u}^n \right), \tag{3}$$

where $\boldsymbol{u}^n$ denotes the velocity at the time level n, $\hat{\boldsymbol{u}}$ is the intermediate solution, Δt is the time step, H contains the non-linear terms, α, γ and ρ are the constants of the Adam–Bashforth/Crank–Nicolson scheme [28, 29]. Equation (3) can be written in delta-form as:

$$\left(1 - \beta \nabla^2\right) \Delta \hat{\boldsymbol{u}} = \left[-\alpha \boldsymbol{\nabla} p^n + \gamma\, H^n + \rho\, H^{n-1}\right] \Delta t + 2\, \beta\, \nabla^2 \boldsymbol{u}^n \tag{4}$$

with $\Delta \hat{\boldsymbol{u}} = \hat{\boldsymbol{u}} - \boldsymbol{u}^n$ and $\beta = \Delta t\, \alpha / (2\, Re)$. Employing a second-order-accurate space discretization with centered finite differences on a Cartesian staggered grid, the matrix associated with the left-hand-side of the equation (4) is sparse and its direct inversion requires, by standard methods, a huge number of operations. Thus, an approximate factorization technique allows the computation of the intermediate non-solenoidal velocity field $\hat{\boldsymbol{u}}$ by means of the solution of simple tri-diagonal matrices [28, 29]. In order to get a divergence-free velocity field, a scalar quantity φ is introduced, such that:

$$\boldsymbol{u}^{n+1} = \hat{\boldsymbol{u}} - \alpha\, \Delta t\, \boldsymbol{\nabla} \varphi\, . \tag{5}$$

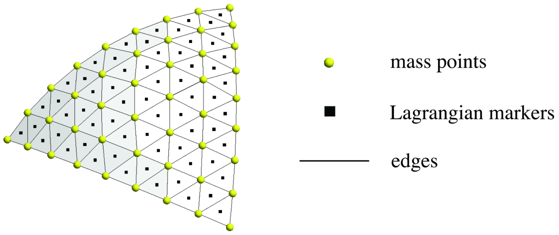

Figure 1: Geometry description by means of triangular elements, whose centroids coincide with the Lagrangian markers.

If the discrete divergence operator is applied to the above equation and the velocity field $\boldsymbol{u}^{n+1}$ is required to be solenoidal, an elliptic equation for φ is obtained,

$$\nabla^2 \varphi = \frac{\boldsymbol{\nabla} \cdot \hat{\boldsymbol{u}}}{\alpha \, \Delta t} \, . \tag{6}$$

The large-banded matrix associated with this equation is reduced to a penta-diagonal matrix using trigonometric expansions (FFTs) in the spanwise direction, and the resulting Helmholtz equations are then inverted using the FISHPACK package [30]. Finally, the pressure field is computed as

$$p^{n+1} = p^n + \varphi - \frac{\alpha \, \Delta t}{2 \, Re} \nabla^2 \varphi \, . \tag{7}$$

2.2. Immersed boundary treatment

In order to overcome the presence of large fluctuations in the hydrodynamic forces arising when extending the direct-forcing formulation of [11] to cases with moving objects, a MLS approach similar to [15] is employed. Following the idea of [13], the forcing is computed on Lagrangian markers laying on the immersed surface, so as to satisfy the boundary condition, and then transferred to the Eulerian grid-points. The structure surface is discretized by means of N_t triangular elements and the Lagrangian markers coincide with the triangles' centroids (figure 1). Given a Lagrangian marker, first the closest Eulerian node is identified, which is centered in a cell with dimension Δx_i in each $i - th$ direction (see figure 2). Then, a support domain is created, centered on the Lagrangian point and extending to $\pm r_i$, with $r_i = 1.5\Delta x_i$. In this way N_e Eulerian points are enclosed in the support domain and associated to the selected marker (27 in three dimensions). A

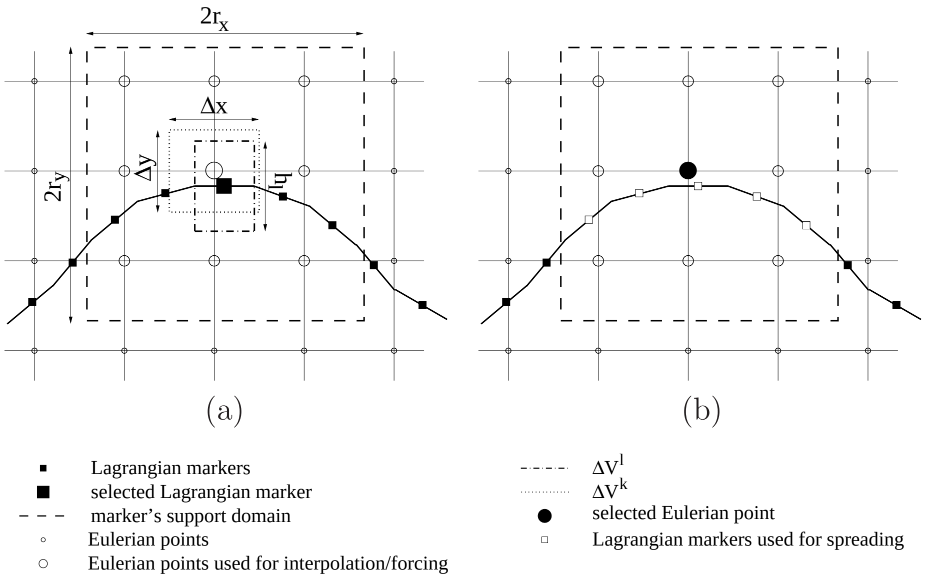

Figure 2: Scheme for IB forcing. (a) Definition of the support domain for a Lagrangian marker. The Eulerian points are involved in the interpolation of the variables at the Lagrangian marker. (b) Lagrangian points associated to a selected Eulerian point. The Lagrangian points are involved in the spreading of the forcing to the Eulerian node.

volume $\Delta V^l = A_l h_l$ is associated to the marker, where A_l is the $l-th$ triangle area and h_l is the local thickness, equal to the average mesh size at the marker location. The MLS approximation is the key ingredient to build a transfer function between the Eulerian and Lagrangian grids, that is able to provide a smooth solution also when applied to arbitrary moving bodies [15]. The reconstruction procedure consists in the following steps:

1. Compute the intermediate velocity $\hat{\boldsymbol{u}}$ from equation (3) in all the Eulerian grid points; this involves also the N_e points of the support domain surrounding a Lagrangian point.
2. Compute the velocity component, $\hat{U}_i$, at each Lagrangian grid point, l, corresponding to the non-solenoidal velocity field. Using the MLS approach, it can be approximated in the support domain as:

$$\hat{U}_i(\boldsymbol{x}) = \boldsymbol{p}^T(\boldsymbol{x})\boldsymbol{a}(\boldsymbol{x}) = \sum_{j=1}^{4} p_j(\boldsymbol{x}) a_j(\boldsymbol{x}) \,, \tag{8}$$

   where $\boldsymbol{p}^T(\boldsymbol{x}) = [1, x, y, z]$ is the linear basis function vector (a cost-efficient choice able to represent the field variation of the variable up to the accuracy of the adopted spatial discretization scheme [15]), $\boldsymbol{a}(\boldsymbol{x})$ is a vector of coefficients and $\boldsymbol{x}$ is the Lagrangian point position. The coefficient vector $\boldsymbol{a}(\boldsymbol{x})$ is obtained minimizing, with respect to $\boldsymbol{a}(\boldsymbol{x})$, the weighted L2-norm defined as:

$$J = \sum_{k=1}^{N_e} W(\boldsymbol{x} - \boldsymbol{x}^k) \left[\boldsymbol{p}^T(\boldsymbol{x}^k) \boldsymbol{a}(\boldsymbol{x}) - \hat{u}_i^k \right]^2 , \tag{9}$$

where $\hat{u}_i^k$ and $\boldsymbol{x}^k$ are the intermediate velocity component and position vector, respetcively, at Eulerian point k in the support domain and $W(\boldsymbol{x} - \boldsymbol{x}^k)$ is a given weight function. This operation leads to

$$\boldsymbol{A}(\boldsymbol{x}) \boldsymbol{a}(\boldsymbol{x}) = \boldsymbol{B}(\boldsymbol{x}) \hat{\boldsymbol{u}}_i^k , \tag{10}$$

with

$$\boldsymbol{A}(\boldsymbol{x}) = \sum_{k=1}^{N_e} W(\boldsymbol{x} - \boldsymbol{x}^k) \boldsymbol{p}(\boldsymbol{x}^k) \boldsymbol{p}^T(\boldsymbol{x}^k) , \tag{11}$$

$$\boldsymbol{B}(\boldsymbol{x}) = \left[W(\boldsymbol{x} - \boldsymbol{x}^1) \boldsymbol{p}^T(\boldsymbol{x}^1) \ldots W(\boldsymbol{x} - \boldsymbol{x}^{N_e}) \boldsymbol{p}^T(\boldsymbol{x}^{N_e}) \right] \tag{12}$$

and

$$\boldsymbol{B} = \left[\hat{u}_i^1 \ldots \hat{u}_i^{N_e} \right]^T . \tag{13}$$

Combining the equations, $\hat{U}_i$ cab be rewritten as:

$$\hat{U}_i(\boldsymbol{x}) = \boldsymbol{\Phi}^T(\boldsymbol{x}) \hat{\boldsymbol{u}}_i^k = \sum_{k=1}^{N_e} \phi_k^l(\boldsymbol{x}) \, \hat{\boldsymbol{u}}_i^k , \tag{14}$$

where $\boldsymbol{\Phi} = \boldsymbol{p}(\boldsymbol{x}) \boldsymbol{A}^{-1}(\boldsymbol{x}) \boldsymbol{B}(\boldsymbol{x})$ is the transfer operator containing the shape function values for marker point l. In this work, the exponential function [31] is used, written as:

$$W(\boldsymbol{x} - \boldsymbol{x}^k) = \begin{cases} e^{-(r_k/\alpha)^2} & r_k \leq 1 \\ 0 & r_k > 1 \end{cases} \tag{15}$$

where $\alpha = 0.3$ and r_k is given by

$$r_k = \frac{|\boldsymbol{x} - \boldsymbol{x}^k|}{r_w} \tag{16}$$

with r_i the size of the support domain previously defined. Note that the shape functions reproduce exactly the linear polynomial contained in their basis and possess the partition of unity property $\sum_{k=1}^{N_e} \phi_k(\boldsymbol{x}) = 1$. Moreover, the field approximation is continuous on the global domain as the MLS shape functions are compatible [31, 15].

3. Calculate the volume force component F_i at all Lagrangian grid points:

$$F_i = \frac{V_i^b - \hat{U}_i}{\Delta t}\,, \tag{17}$$

   where V_i^b is the velocity component on the marker to be imposed as a boundary condition.

4. Transfer back F_i to the k Eulerian grid points associated with each Lagrangian grid point, using the same shape functions employed in the interpolation procedure, properly scaled by a factor c_l, which is determined by imposing that the total force acting on the fluid is not changed by the transfer [15]:

$$f_i^k = \sum_{l=1}^{N_t} c_l\, \phi_k^l F_i^l\,; \tag{18}$$

   in the above equation f_i^k is the volume force component in the Eulerian point k and N_t indicates the number of Lagrangian points associated with the Eulerian point k(i.e. Lagrangian point whose support domain contains the selected Eulerian point, as shown on the right in figure 2). The scaling factor c_l is obtained considering a forcing volume associated with each Eulerian point equal to the Eulerian cell volume, ΔV^k, and the forcing volume associated with the Lagrangian marker previously defined, and imposing that the total force acting on the fluid is not changed by the transfer:

$$\sum_{k=1}^{N_e,tot} f_i^k \Delta V^k = \sum_{l=1}^{N_t} F_i^l \Delta V^l\,. \tag{19}$$

   Rearranging the terms, one has:

$$c_l = \frac{\Delta V^l}{\sum_{k=1}^{N_e} \phi_k^l \Delta V^k} \tag{20}$$

The transfer operators conserve momentum on both uniform and stretched grids, while the equivalence of total torque between the Eulerian and Lagrangian grids are guaranteed for uniform grids, with minimal errors for low stretched grids (about 10%) [15].

5. Correct the intermediate velocity so as to impose the correct boundary conditions on the immersed body:

$$\boldsymbol{u}^* = \hat{\boldsymbol{u}} + \Delta t\, \boldsymbol{f}\,, \tag{21}$$

   where $\boldsymbol{f}$ is the volume force at Eulerian cells, obtaining a velocity field that is not divergence-free and that will be projected into a divergence-free space by applying the pressure correction which satisfies the Poisson equation (6).

2.3. Rigid body equations

The motion of the rigid body immersed in the fluid is governed by the Newton–Euler equations imposing the equilibrium of translation and rotation:

$$M\frac{d\boldsymbol{V}}{dt} = \boldsymbol{F}_{tot}\,, \qquad \boldsymbol{V} = \frac{d\boldsymbol{X}}{dt}\,, \tag{22}$$

$$[I]\,\frac{d\boldsymbol{\Omega}}{dt} = \boldsymbol{T}_{tot}\,, \qquad \boldsymbol{\Omega} = \frac{d\boldsymbol{\Theta}}{dt}\,. \tag{23}$$

In the equations above, M and $[I]$ are the mass and inertia tensor of the body, $\boldsymbol{V}$ and $\boldsymbol{X}$ its baricentre's velocity and position, $\boldsymbol{\Omega}$ and $\boldsymbol{\Theta}$ its angular velocity and position, respectively, and $\boldsymbol{F}_{tot}$ and $\boldsymbol{T}_{tot}$ are the total force and moment acting on the body. The total force and moment include the hydrodynamics contributions, the gravity forces, if present, and any other additional force depending on the problem. Concerning the hydrodynamics loadings, the overall contribution is obtained integrating over the body's surface the pressure and viscous stresses as explained in section 2.5.

2.4. Spring network model for deformable bodies

A simple spring network model is adopted for describing the dynamics of deformable bodies, based on the minimum energy concept [25]. The structural model is built considering the triangulated network of N_s springs (edges), forming N_t triangles. The mass of the structure is concentrated on the N_v vertices of the triangles, uniformly distributed on the surface. The potential energy of the system includes in-plane elastic terms, combined with bending energy and additional constraints for surface area and volume conservations.

The simplest elastic energy model is described by:

$$W^e = \frac{1}{2} k_e x^2 \tag{24}$$

where W^e is the related potential energy, $x = l - l_0$, l is the length of the stretched spring, l_0 is the length of the spring in the *stress-free* configuration and k_e is the elastic constant. The elastic constant for a given edge of length l is obtained by the model of [32]:

$$k_e = \frac{Eh \sum_i A_i}{l^2}\,, \tag{25}$$

where E is the Young's modulus for the material, h is the membrane thickness (here assumed uniform for all triangles), i identifies the triangles sharing the selected edge (here two triangles) and A_i is the triangle area. Taking the derivative of the potential energy with respect to displacements, the nodal forces corresponding to the elastic energy for nodes 1 and 2 connected by an edge (figure 3) are obtained by:

$$\mathbf{F}_1^e = -k_e(l - l_0)\frac{\mathbf{r}_{12}}{l} \tag{26}$$

$$\mathbf{F}_2^e = -k_e(l - l_0)\frac{\mathbf{r}_{21}}{l} \tag{27}$$

where $\mathbf{r}_{ij} = \mathbf{r}_i - \mathbf{r}_j$, with $\mathbf{r}_i$ position vector of the node i and $l = |\mathbf{r}_{21}|$ is the actual edge length.

The out-of-plane deformation of two adjacent faces sharing an edge is modeled by means of a bending spring, as shown in figure 3. Four nodes are involved in the energy term. Considering a null reference curvature of the local surface, the free elastic energy in discrete form is given by [33]:

$$W^b = k_b(1 - \mathbf{n}_1 \cdot \mathbf{n}_2) = k_b[1 - cos(\theta)] \tag{28}$$

where $\mathbf{n}_1$ and $\mathbf{n}_2$ are the surface vectors normal to the triangular elements shared by the edge, θ is the angle between $\mathbf{n}_1$ and $\mathbf{n}_2$ and k_b is the bending constant. In case of a surface with non-zero reference curvature in the stress-free configuration, the bending energy can be written as

$$W^b = k_b[1 - cos(\theta - \theta_0)] \tag{29}$$

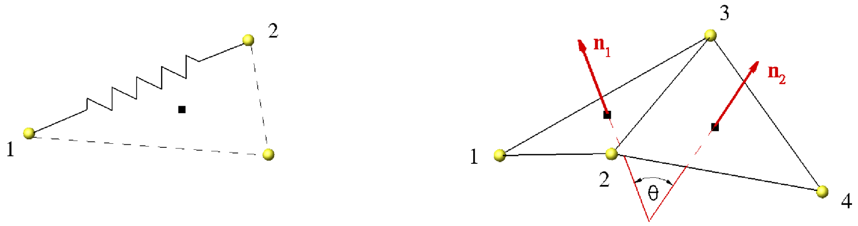

Figure 3: Left: sketch of the two nodes (vertices of an edge) involved in the elastic spring model. Right: four nodes (belonging to the two triangles sharing an edge) involved in the bending spring model.

where θ_0 is the value of θ in the stress-free configuration. The bending constant k_b is related to the equivalent averaged bending modulus of the structure, B, as [34]:

$$k_b = B\frac{2}{\sqrt{3}}\,. \tag{30}$$

The nodal forces corresponding to the bending energy are obtained as (see figure 3):

$$\mathbf{F}_1^E = \beta_b\left[b_{11}\left(\mathbf{n}_1 \times \mathbf{r}_{32}\right) + b_{12}\left(\mathbf{n}_2 \times \mathbf{r}_{32}\right)\right] \tag{31}$$

$$\mathbf{F}_2^E = \beta_b\left[b_{11}\left(\mathbf{n}_1 \times \mathbf{r}_{13}\right) + b_{12}\left(\mathbf{n}_1 \times \mathbf{r}_{34} + \mathbf{n}_2 \times \mathbf{r}_{13}\right) + b_{22}\left(\mathbf{n}_2 \times \mathbf{r}_{34}\right)\right] \tag{32}$$

$$\mathbf{F}_3^E = \beta_b\left[b_{11}\left(\mathbf{n}_1 \times \mathbf{r}_{21}\right) + b_{12}\left(\mathbf{n}_1 \times \mathbf{r}_{42} + \mathbf{n}_2 \times \mathbf{r}_{21}\right) + b_{22}\left(\mathbf{n}_2 \times \mathbf{r}_{42}\right)\right] \tag{33}$$

$$\mathbf{F}_4^E = \beta_b\left[b_{11}\left(\mathbf{n}_1 \times \mathbf{r}_{23}\right) + b_{22}\left(\mathbf{n}_2 \times \mathbf{r}_{23}\right)\right] \tag{34}$$

with

$$b_{11} = -\frac{cos(\theta)}{|\mathbf{n}_1|^2}; \qquad b_{12} = \frac{1}{|\mathbf{n}_1||\mathbf{n}_2|}; \qquad b_{22} = -\frac{cos(\theta)}{|\mathbf{n}_2|^2}; \tag{35}$$

and

$$\beta_b = k_b\frac{sin(\theta)cos(\theta_0) - cos(\theta)sin(\theta_0)}{\sqrt{1 - cos^2(\theta)}} \tag{36}$$

Additional energy terms can be added, in order to give a constraint on the area (of each triangle and/or global area) and enclosed volume (if the surface is closed) changes [25, 35].

For each node of the structure the dynamic equation of motion is solved, considering the internal and external forces:

$$m_p\ddot{\mathbf{x}} = \mathbf{F}^{\mathbf{ext}} + \mathbf{F}^{\mathbf{int}} = \mathbf{F} \tag{37}$$

where m_p is the mass of the node, $\mathbf{F^{ext}}$ are the external forces on the nodes (i.e. hydrodynamic loads, gravity forces) and $\mathbf{F^{int}}$ are the internal forces previously defined. A damping term could be added on the left hand side in order to take into account for the viscoelasticity of the structure.

A comment is necessary regarding the adopted structural model. Spring network models are discrete, defining the elastic forces on the vertices based on edges' length and triangles' reciprocal angle variations, as well as other constraints such as area and volume variations. This makes the models far from the continuum model, which assumes the homogeinity of the mechanical properties throughout the membrane surface. Therefore, the evaluation of the spring constants, in order to mimic the continuum model, may not be trivial. There are several studies in literature aiming at defining a link between spring networks and continuum mechanics. Gelder [32] showed that such models can not represent a continuum membrane model exactly, but proposed an alternative formulation to evaluate the spring constant in order to accurately represent an isotropic continuum membrane. Delingette [36] introduced a novel spring type (bi-quadratic spring with tensile and angular stiffness), based on finite strain mechanics and with great potential for accurate non-linear membrane simulations. In [37], the effect of network parameters, i.e. mesh, spring type and surface constraint have been studied, with particular attention to the modeling of a red blood cell's (RBC) membrane. They showed that an isotropic spring network is mechanically isotropic in small deformation while a spring network with high randomness tend to be mechanically isotropic even in large deformation and that the network elasticity is independent of the density of the network mesh. All spring networks are indeed vulnerable against surface area dilation. In conclusion, the mechanical behavior of such models is conditionally equivalent to that of continuum-based membrane models [37]. Different spring models can be used, e.g., linear, truss, neo-Hookean, worm-like-chains. Several application have been presented in literature, especially for RBC mechanics [38, 39, 34, 40, 35, 37, 41], showing that the model can give sufficiently accurate results in modeling the RBC membrane. Here, we decided to adopt a spring network model for its very simple formulation and reduced computational cost. Moreover, one has to take into account that in several biological applications the uncertainty in determining material properties could be larger than the discrepancies between spring network and continuum models. In any case, there is no limitation of the proposed method in replacing this simplified solver by a more accurate, and computationally more expensive, finite element membrane solver [27].

As an example of a more complex biological tissue, the simulation of the dynamics of a bioprosthetic aortic valve in a pulsatile flow is presented in section 3.8. During the cardiac cycle, the aortic valve leaflets open and close by bending, undergoing large deformation with change of curvature, and resist diastolic pressure experiencing in-plane stresses. This complex behavior is strictly related to the leaflet internal structure, therefore a proper specification of the material properties combined with a realistic mechanical model are crucial. Three layers compose the aortic leaflet tissue, each having different characteristics. The different fiber orientation is responsible of mechanical anisotropy: the circumferential elastic modulus of human aortic valve tissue can be 6-8 times larger than the one evaluated in the radial direction [42]. Moreover, the material response to large strains is highly nonlinear and hyperelastic. Here, the presented banding model is adopted, along with a simplified nonlinear anisotropic material behavior for the in-plane stress. As shown in [43], using a continuum model, the in-plane response of the aortic valve tissue can be described by means of Fung-type constitutive law:

$$S_{ij} = \frac{\partial W}{\partial E_{ij}} \tag{38}$$

where S_{ij} and E_{ij} are the components of the second Piola–Kirchhoff stress tensor and Green strain tensor, respectively, i and j are the indices representing the two principal directions, and W is the strain energy density. W can be formulated as [44]:

$$W = \frac{c}{2}(e^{Q} - 1) \tag{39}$$

with

$$Q = A_1 E_{11}^2 + A_2 E_{22}^2 + 2A_3 E_{11} E_{22} + A_4 E_{12}^2 + 2A_5 E_{11} E_{12} + 2A_6 E_{22} E_{12} \tag{40}$$

The values of the constants are obtained by fitting previously published biaxial esperiments on normal aortic valve tissue [43], and are here reported for reference, $c = 9.7\,Pa$, $A_1 = 49.558$, $A_2 = 5.2871$, $A_3 = -3.124$, $A_4 = 16.031$, $A_5 = -0.004$ and $A_6 = -0.02$. With the aim of using a network spring model instead of a continuum one, as done in [43] (where the only structural solver is considered), the anisotropic behavior is simplified considering only two stress-strain curves, corresponding to equibiaxial loading (one curve for

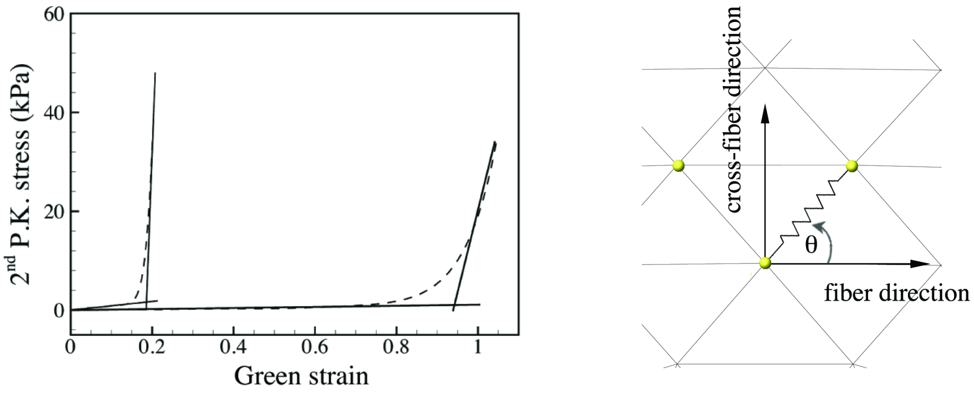

(a) (b)

Figure 4: Bilinear relationship approximating the hyperelastic behavior of aortic valve material, as in [43].

the fiber fiber direction and one for the cross-fiber direction) of the aortic valve tissue (see figure 4a). The nonlinear behavior in both directions is further simplified approximating the curves by means of a piecewise linear fit consisting of a segment of slope m_1 passing through the origin and a second segment of slope m_2 intersecting the first segment at some critical value of Green strain (indicated as stretch ratio λ^*). The undeformed (stress-free) configuration of the valve leaflet is taken as a reference for evaluating the angle between the single spring (edge) direction with respect to the material fiber direction (horizontal direction in this work), θ, as indicated in figure 4b. Then, for each edge at a given angle θ, intermediate between the the fiber and cross-fiber directions, the slope parameter is calculated by (m_1 for example):

$$m_1(\theta) = \sqrt{m_{1f}^2 cos^2\theta + m_{1c}^2 sin^2\theta} \tag{41}$$

where m_{1f} and m_{1c} are the initial slopes in the fiber and cross-fiber directions, respectively. The same formulation is adopted to evaluate the other parameters, m_2 and λ^*, based on the angle θ in the stress-free configuration of the mesh. In such a way, the line slopes as well as the stretch ratio is stored for each spring. The Van Gelder [32] approach is employed for calculating elastic constant, k_e, where in place of Young's modulus, the evaluated slopes of the bilinear model, $m1$ or $m2$ are used, depending on whether the actual deformation of the spring corresponds to a value of stretch less than or greater than λ^* [43]. Two elastic constants are obtained (form small and large displacements, k_{e1} and k_{e2}). The elastic force on one node of the spring (e.g. node 1 in figure 3) is evaluated by:

$$\mathbf{F}_1^E = -k_{e1}(l - l_0)\frac{\mathbf{r}_{12}}{l} \tag{42}$$

for springs with stretch magnitude less than λ^*, or

$$\mathbf{F}_1^E = -\left[k_{e1}l_0(\lambda^* - 1) + k_{e2}(l - \lambda^* l_0)\right]\frac{\mathbf{r}_{12}}{l} \tag{43}$$

for springs with stretch magnitude freater than λ^*.

2.5. Force and moment evaluation

The forces and moments in equations (22),(23) and (37) are calculated by considering the pressure and viscous stresses over the immersed body surface. Given the triangular discretization of the surface, the local force contribution is evaluated for each triangular element.

For the case of a closed surface, representing a rigid or deformable solid, the single contributions to the force and moment are evaluated for each triangular element, l:

$$\boldsymbol{F}_l(t) = (\boldsymbol{\tau}_l \cdot \boldsymbol{n}_l - p_l \boldsymbol{n}_l)\, S_l\,, \tag{44}$$

$$\boldsymbol{M}_l(t) = \left[(\boldsymbol{\tau}_l \cdot \boldsymbol{n}_l - p_l \boldsymbol{n}_l) \times \boldsymbol{r}_l\right] S_l\,, \tag{45}$$

where $\boldsymbol{\tau}_l$ and p_l are the viscous stress tensor and pressure, evaluated at the centroid of each triangle (location of the Lagrangian marker, l), $\boldsymbol{n}_l$ and S_l are the unit outward normal vector and area of each triangle, while $\boldsymbol{r}_l$ is the position vector of the marker with respect to its baricentre. In order to evaluate the pressure p_l and the velocity derivatives, for each Lagrangian marker a probe is created along its normal direction, at a distance h_l, equal to the averaged local grid size. Using the same MLS formulation described above, pressure and velocity are evaluated at the probe location. Then, the pressure on the markers is calculated as:

$$p_l = p_l^* + \frac{D\boldsymbol{u}_l}{Dt} \cdot \boldsymbol{n}_l \tag{46}$$

where p_l^* is the pressure on the probe and the second term of the right hand side, involving the acceleration of the marker, $D\boldsymbol{u}_l/Dt = d\boldsymbol{v}_l/dt$, comes from the evaluation of the pressure gradient in the normal direction by the

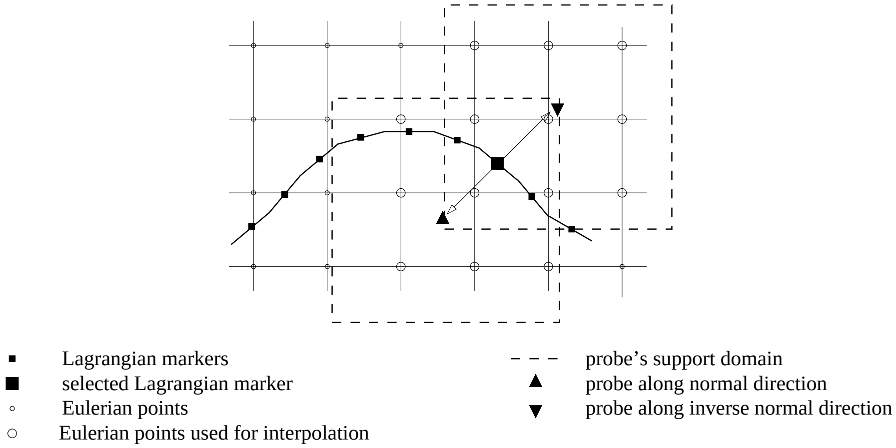

Figure 5: Scheme for IB forces evaluation.

momentum equation [14]. Concerning the velocity derivatives on the body surface, these are considered equal to the velocity derivatives evaluated at the probes, that is equivalent to assume a linear variation of the velocity near the body. This is consistent with the second-order accuracy of the space discretization scheme and turns out to be a good approximation provided that the grid is sufficiently refined near the body. For the case of rigid bodies, the total force and moment to be considered in equations (22) and (23) are obtained by summing all the contributions of equations (44) and (45) over the N_t triangles describing the immersed surface; on the other hand, in case of deformable bodies, the $\boldsymbol{F}_l(t)$ is equally distributed among the three nodes of the $l-th$ triangle: the total hydrodynamic force acting on each triangle vertex is obtained summing all the contributions of the triangles sharing that node.

In the case of vesicles or open surfaces, one has to account for the forces due to the presence of the fluid on both sides of the surface, namely, also in the opposite normal direction, for each triangle, in order to obtain the total force:

$$\boldsymbol{F}_l(t) = S_l\left[\left(\boldsymbol{\tau}_l^+ - \boldsymbol{\tau}_l^-\right)\cdot\boldsymbol{n}_l - (p_l^+ - p_l^-)\boldsymbol{n}_l\right]\,, \tag{47}$$

$$\boldsymbol{M}_l(t) = S_l\left[\left(\boldsymbol{\tau}_l^+ - \boldsymbol{\tau}_l^-\right)\cdot\boldsymbol{n}_l - (p_l^+ - p_l^-)\boldsymbol{n}_l\right]\times\boldsymbol{r}_l\,, \tag{48}$$

where $^+$ and $^-$ quantities are evaluated on the probes along the positive and negative n_l directions, respectively (see figure 1). It is worth noting that with the present method one can sustain large pressure differences across

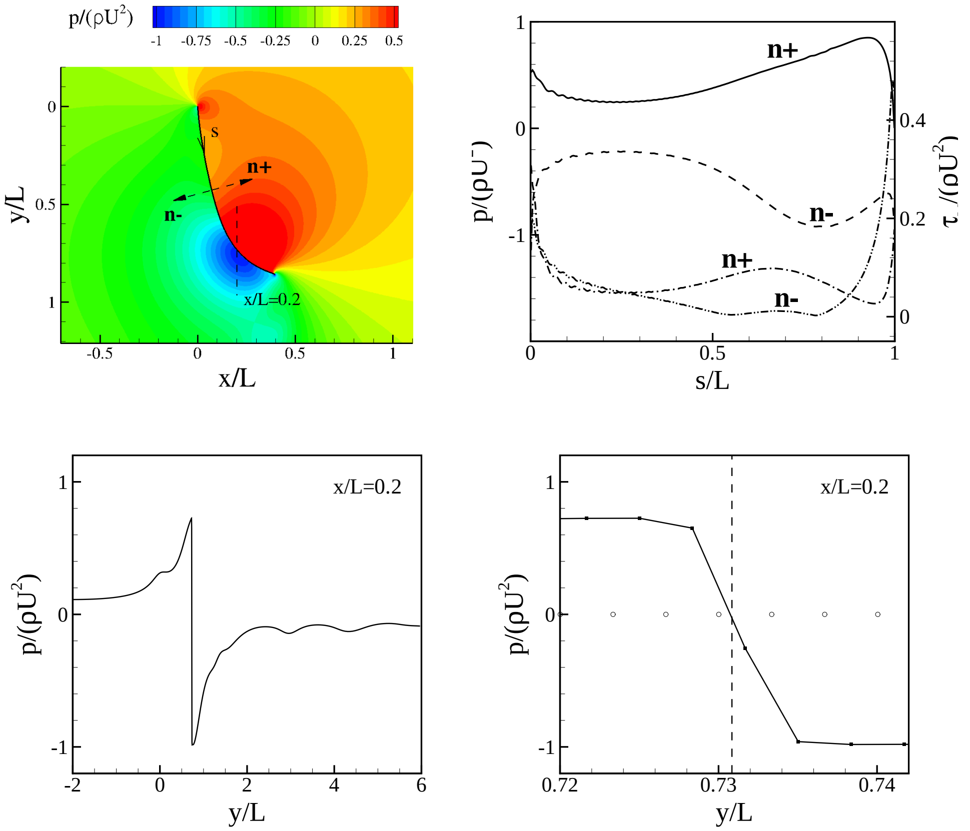

Figure 6: Pressure (red lines) and streamwise velocity (blue lines) distributions on the centerline of the computational domain for the case of a uniform flow past a fixed vertical plate.

one Eulerian cell.

As an example, the results for the flow past a fixed, *zero-thickness* vertical plate is shown in figure 6. The flow comes from left to right with velocity U and impacts on a plate of height L, with $Re = \rho_f UL/\mu = 200$. The computational domain is $[-2L, 6L] \times [-4L, 4L]$. The center of the plate is placed at $[0.5L, 0]$. Inlet and outlet boundary conditions are imposed on the vertical boundaries, while free-shear wall conditions are imposed for the horizontal boundaries. A non uniform grid of 671×747 nodes is used with a uniform grid spacing of $0.01L$ in the vicinity of the plate. The Lagrangian markers are distributed uniformly onto the plate surface, with a spacing of about 0.7 the local Eulerian grid size in that area. Figure 6 shows the pressure and streamwise velocity distributions on the centerline of the computational domain. The pressure difference across the plate is shown, captured in one grid cell along the streamwise direction (figure 6, left). Figure 6 shows an instantaneous field of the pressure contours and the pressure distribution along the plate considering the upstream and downstream normal probe directions.

2.6. Fluid-structure-interaction strategy

The evaluation of the flow and body motion at each time step is carried out by means of an implicit strongly coupled approach to ensure convergence and to allow the use of larger time steps, since the prediction of the flow field and of the hydrodynamic loads requires the knowledge of the motion of the bodies and vice–versa [45]. The adopted approach is based on Hamming's 4th order modified predictor-corrector method with mop-up correction [26]. For the case of a rigid body, $\ddot{\mathbf{x}}$, $\dot{\mathbf{x}}$ and $\mathbf{x}$ represent the acceleration, velocity and position, respectively, of the body's baricentre (in that case $m = M$ is the mass of the entire body), and the same approach is adopted to evaluate angular acceleration, velocity and position (considering the inertial tensor). On the other hand, for the case of deformable body, $\ddot{\mathbf{x}}$, $\dot{\mathbf{x}}$ and $\mathbf{x}$ represent acceleration, velocity and position, respectively, of each triangle's vertex and $m = m_p$ is the mass on each node, obtained by uniformly distributing the total mass of the structure over the N_v nodes. Subscripts indicate the time instant.

For each time step,

1. Predictor:
    - $\ddot{\mathbf{x}}_n = \mathbf{F}_n/m$
    - $\dot{\mathbf{x}}^p_{n+1} = \dot{\mathbf{x}}_{n-3} + \frac{4}{3}\Delta t\,(2\ddot{\mathbf{x}}_n - \ddot{\mathbf{x}}_{n-1} + 2\ddot{\mathbf{x}}_{n-2})$
    - $\dot{\mathbf{x}}^m_{n+1} = \dot{\mathbf{x}}^p_{n+1} - \frac{112}{121}\,(\dot{\mathbf{x}}^p_n - \dot{\mathbf{x}}^c_n)$
    - $\mathbf{x}^p_{n+1} = \mathbf{x}_{n-3} + \frac{4}{3}\Delta t\,(2\dot{\mathbf{x}}_n - \dot{\mathbf{x}}_{n-1} + 2\dot{\mathbf{x}}_{n-2})$
    - $\mathbf{x}^m_{n+1} = \mathbf{x}^p_{n+1} - \frac{112}{121}\,(\mathbf{x}^p_n - \mathbf{x}^c_n)$
    - Solve flow and structure (if deformable body) equations, using the predicted structural node position and velocity and evaluate $\mathbf{F}^1_{n+1}$
2. Corrector: do loop on k, while convergence is achieved:
    - $\ddot{\mathbf{x}}^k_{n+1} = \mathbf{F}^k_{n+1}/m$
    - $\dot{\mathbf{x}}^c_{n+1} = \frac{1}{8}\,(9\dot{\mathbf{x}}_n - \dot{\mathbf{x}}_{n-2}) + \frac{3}{8}\Delta t\,\left(2\ddot{\mathbf{x}}^k_{n+1} + 2\ddot{\mathbf{x}}_n - \ddot{\mathbf{x}}_{n-1}\right)$

- $\mathbf{x}^c_{n+1} = \frac{1}{8}\left(9\mathbf{x}_n - \mathbf{x}_{n-2}\right) + \frac{3}{8}\Delta t\left(2\dot{\mathbf{x}}^k_{n+1} + 2\dot{\mathbf{x}}_n - \dot{\mathbf{x}}_{n-1}\right)$
- Check for converge of the structure equations: $|\mathbf{x}^{k+1}_{n+1} - \mathbf{x}^k_{n+1}| < \epsilon$
- If converged,
  - $\dot{\mathbf{x}}_{n+1} = \dot{\mathbf{x}}^c_{n+1} + \frac{9}{121}\left(\dot{\mathbf{x}}^p_{n+1} - \dot{\mathbf{x}}^c_{n+1}\right)$
  - $\mathbf{x}_{n+1} = \mathbf{x}^c_{n+1} + \frac{9}{121}\left(\mathbf{x}^p_{n+1} - \mathbf{x}^c_{n+1}\right)$
  - Solve flow and structure equations (if deformable body), using the new structural node position and velocity and evaluate $\mathbf{F}_{n+1}$
- If not converged,
  - Solve flow and structure equations (if deformable body), using the actual structural node position and velocity and evaluate $\mathbf{F}^{k+1}_{n+1}$
  - repeat the corrector procedure until convergence

In order to provide the previous time steps solutions needed, lower-order method are employed for the first time steps of integration. The tolerance ϵ considered in this work is equal to 10^{-7}, and the method converges in $2-8$ iterations, depending on the problem complexity and structure mass and elastic properties. In the case of large accelerations, under-relaxation could be considered in order to maintain the system stable.

3. Results

3.1. Sedimentation of an elliptic particle

The dynamics of a single two-dimensional elliptic particle sedimenting in a confined channel is considered here to validate the FSI procedure. A systematic verification study is also performed to check the order of accuracy of the algorithm. The problem is configured as an elliptic particle with aspect ratio $\alpha = a/b = 2$, where a and b are the major and minor axes, respectively, as shown in Figure 7. The confined channel has width L, with a blockage ratio $\beta = L/a = 4$. The density ratio, $\gamma = \rho_s/\rho_f$ is set equal to 1.1, where ρ_s and ρ_f are the particle and fluid densities, respectively. The computational domain is $[0, L] \times [0, 7L]$ in X and Y directions, respectively, with the gravity g pointing in the negative Y direction. The particle starts falling with the centroid in $(0.5L, 6L)$, with an initial angle of $\theta_0 = 45°$, to break the symmetry. Considering the terminal settling velocity of the particle, V_T, the major axis of the ellipse and the fluid kinematic viscosity, ν, the Reynolds number is $Re_T = V_T a/\nu = 12.5$, while the Froude number is $Fr_T = V_T/\sqrt{ga} = 0.126$. In physical units, the major axis of the ellipse is $0.1\,cm$ and the kinematic viscosity of the fluid is $0.01\,cm^2/s$ [46]. A slip wall boundary condition is applied at the top boundary and all other boundaries are treated as no-slip wall boundaries. Eight uniform Cartesian grids are used with nodes: 81×561, 101×701, 134×934, 161×1121, 201×1401, 267×1867, 401×2801, 801×5601, corresponding to an Eulerian grid spacing, $\Delta h/a$, of 0.05, 0.04, 0.03, 0.025, 0.02, 0.015, 0.01, 0.005, respectively. A uniform Lagrangian marker spacing is adopted for all the cases, equal to 0.77 the Eulerian grid size. With the aim of investigating the overall numerical accuracy in both space and time, the time steps for each grid is chosen in order to mantain a constant ratio between the grid spacing and time step, $\Delta h/\Delta t = 5U_t$. In Figure 7 the present results in terms of particle settling velocity, trajectory (location of center of mass) and orientation for the grids with $\Delta h/a$ equal to 0.04, 0.02 and 0.01 are shown, compared with the numerical results obtained by [46] by means of a finite-element method. The particle settles into the center of the channel ($x/L = 0.5$) with a constant velocity, and sediments in a horizontal configuration ($\theta = 0$). The agreement of the results is very good for the three grids considered. For the accuracy study, the solution from the finest grid, 801×5601, is used as reference. Three relative errors are defined, for the terminal position and velocity at time $t = 0.8\,s$, namely $\epsilon_P = [(Y - Y^{ref})/Y^{ref}]_{t=0.8s}$ and $\epsilon_V = [(V_Y - V_Y^{ref})/V_Y^{ref}]_{t=0.8s}$, respectively, and for the time averaged value of the terminal velocity in the interval $t = [0.8, 1.6]\,s$, namely $\epsilon_{<V>} = (< V_Y > - < V_Y^{ref} >)/ < V_Y^{ref} >$. The relative errors are reported versus grid spacing in Figure 8, showing a first-order convergence rate for the coarser grids and an evident overall second-order accuracy on finer grids.

3.2. Fluttering and tumbling of a plate

The falling dynamics of a plate is considered in order to test the ability of the proposed technique to capture the transition between tumbling and fluttering. Previous experimental studies [47] on thin flat strips falling in a vertical cell have shown that the transition is regulated by the Reynolds and Froude numbers. A two-dimensional elliptical plate is considered, with a thickness-to-length ratio h/L equal to 0.125, as shown in Figure 9a. The Reynolds number, defined as $Re = U_0 L/\nu$, is equal to 140 for the fluttering and to 420 for the tumbling case, where $U_0 = \sqrt{2(\rho_s/\rho_f - 1)hg}$ is the

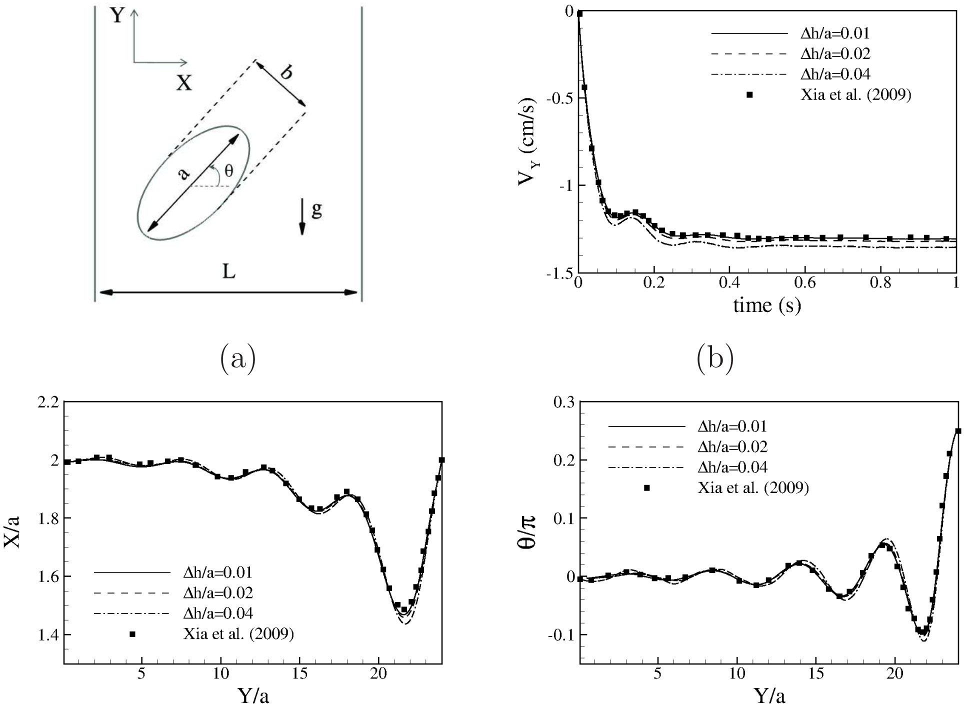

(a) (b)

(c) (d)

Figure 7: (a) Geometrical parameters for the elliptic particle sedimenting in a confined channel, with $Re_T = 12.5$, $Fr_T = 0.126$, $\alpha = 2$, $\beta = 4$, $\gamma = 1.1$; (b) sedimentation velocity; (c) location of center of mass; (d) orientation of the particle. Present numerical results (lines) are compared with finite-elements numerical results of [46] (symbols).

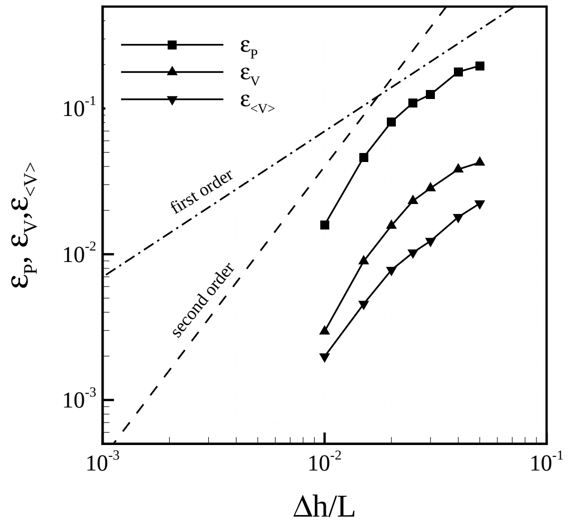

Figure 8: Systematic study of accuracy for an elliptic particle sedimenting in a confined channel, with $Re_T = 12.5$, $Fr_T = 0.126$, $\alpha = 2$, $\beta = 4$, $\gamma = 1.1$.

characteristic speed and g the module of gravitational acceleration, the latter pointing in the negative Y direction. The modified Froude number, defined as $Fr = \sqrt{M/(\rho_f L^2)}$ for a two-dimensional body, with M the mass of the plate per unit width, is equal to 0.45 and 0.89 for the fluttering and tumbling cases, respectively, as done in the computational work of [48]. The computational domain considered is $[0, 30L] \times [0, 30L]$ in X and Y directions, respectively. The particle starts falling with the centroid in $(15L, 28L)$ for the fluttering cases, and in in $(25L, 28L)$ for the tumbling ones, with two different initial angles per case, θ_0, of $45°$ and $-75°$. Slip wall boundary conditions are applied at the top boundary and at the vertical boundaries of the domain, while a no-slip boundary condition is imposed at the bottom boundary. A uniform computational grid is used, with 2300×2300 nodes, with an Eulerian grid spacing of about $0.013L$, and a uniform Lagrangian marker spacing of $0.01L$. A constant time step of $\Delta t = 5 \cdot 10^{-3}\, L/U_0$ is used. The trajectories of the plates are reported in figure 9. The two plates show a very similar steady fluttering, regardless their initial angle, with a different transient process for the case with $\theta_0 = -75°$. Concerning the tumbling behavior, the plate with $\theta_0 = 45°$ shows a longer transient period in which it starts fluttering and then falls tumbling. The descending angle with respect to the horizontal

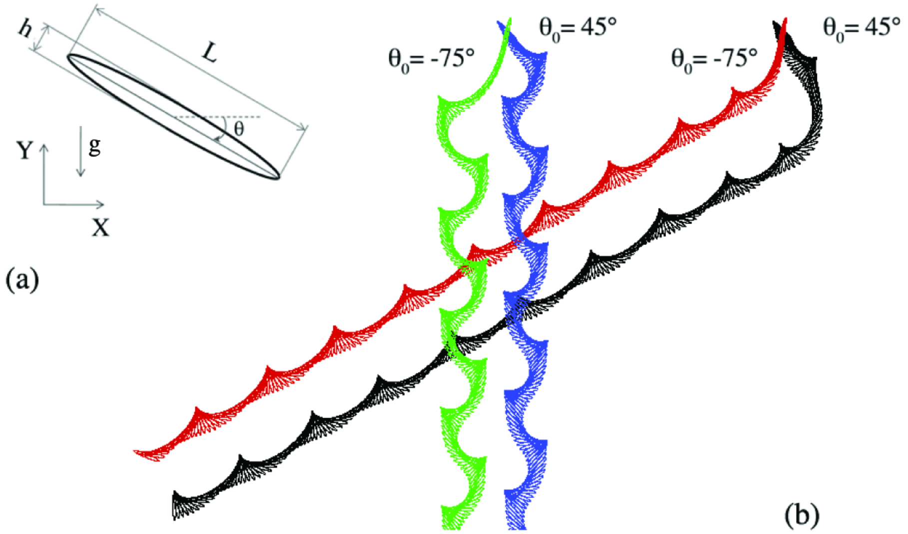

Figure 9: (a) Geometrical parameters for the plate falling in a quiescent fluid. (b) Overlapping of plate positions for fluttering ($Re = 140$, $Fr = 0.45$) and tumbling ($Re = 420$, $Fr = 0.89$) plates. Black: tumbling case, $\theta_0 = 45°$; red: tumbling case, $\theta_0 = -75°$; blue: fluttering case, $\theta_0 = 45°$; green: fluttering case, $\theta_0 = -75°$ (Colour online).

direction is the same in the two tumbling cases. Figure 10 shows the horizontal and vertical force coefficients, calculated by $C_i = 2F_i/\rho_f U^2 L$, where F_i is the hydrodynamic force acting on the plate in the $i - th$ direction, as well as the two velocity components for the fluttering and tumbling cases with $\theta_0 = 45°$, compared with the numerical results of [48]. A very good agreement is obtained for all the cases.

3.3. Particle migration in a planar Couette flow

The two-dimensional motion of a single circular particle in a shear flow is considered, in order to evaluate the sensibility of the code in capturing the particle lateral migration, which is due to a vertical velocity component that is very small compared with the horizontal one (slow migration). The difference in the relative velocity across a solid particle may drive it to move laterally since the side with a higher relative velocity may lead to a lower pressure. In [49, 50], the authors suggested that three mechanisms are responsible for the motion in a linear shear flows: wall lubrication repulsion; inertial lift due to shear slip and lift due to particle rotation. An accurate evaluation of the forces is necessary to properly evaluate the correct dynamics. The circular particle has radius r and the width of the channel is $h = 8r$. The computational domain considered is $[-100r, 100r] \times [0, 8r]$ in the x and y directions, respectively. Periodic boundary conditions are imposed in the horizontal direction. In the vertical direction, no-slip wall is imposed at the lower surface of the domain, while the upper surface has an imposed velocity, U_h (see figure 11). The bulk Reynolds number considered is $Re_b = U_h h/\nu = 40$, which corresponds to a particle Reynolds number $Re_p = U_h r^2/(\nu h) = 0.625$ that does not satisfy the small-Re_p condition required for validity of perturbation theories of the viscous type or inertial type [49]. The particle is considered neutrally buoyant. Two initial conditions are considered, with the particle vertical position equal to $h/4$ and $3h/4$. Here we consider the initial value of the difference between the particle streamwise velocity and the undisturbed velocity at the center of the particle, namely *slip velocity* (δU), $\delta U_{init} = 0$. Ho and Leal [51] and later Vasseur and Cox [52] showed that in conditions of low Reynolds number, neutrally buoyant particles in a simple shear Couette flow will migrate toward the center plane because of the influence of the walls (agreeing with experimental observations by Halow and Wills [53]). In the present simulations for the Couette flow, the particles are observed to migrate toward the median plane of the channel, as shown in Figure 12, regardless of their initial position, with a good agreement with the results

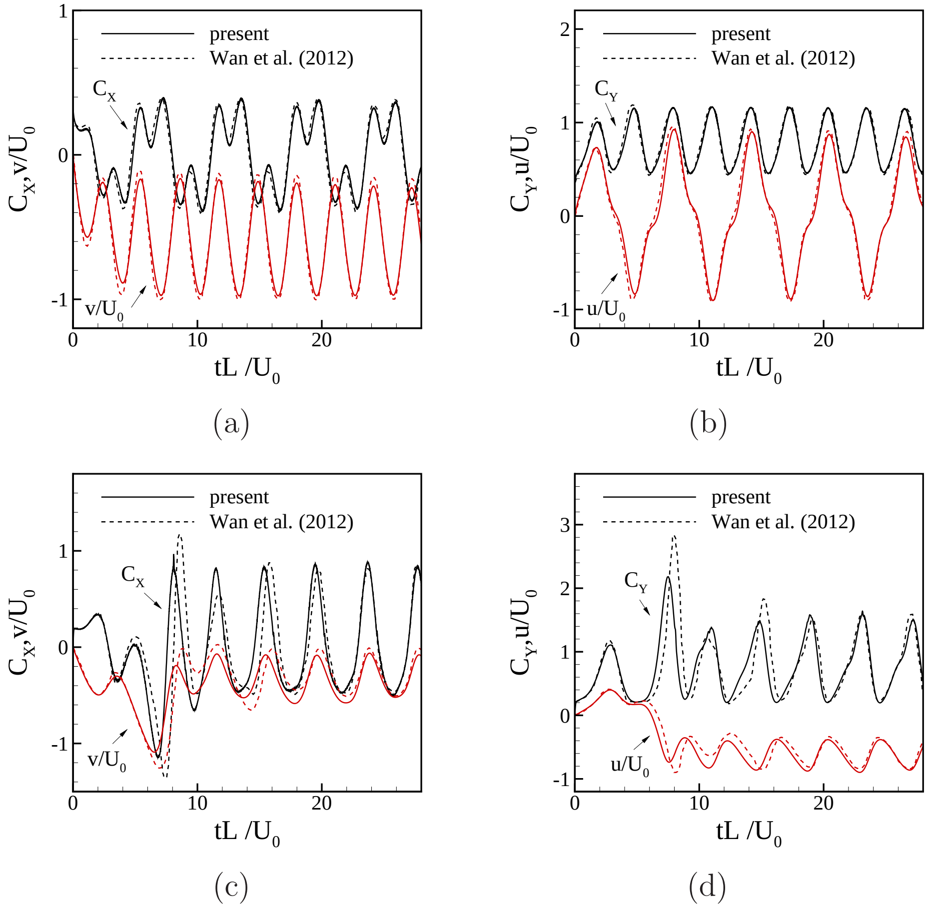

Figure 10: Top: fluttering case with $Re = 140$, $Fr = 0.45$, $\theta_0 = 45°$. (a) Horizontal force coefficient, C_x, and vertical velocity component, v; (b) vertical force coefficient, C_y, and horizontal velocity component, u. Bottom: tumbling case with $Re = 420$, $Fr = 0.89$, $\theta_0 = 45°$. (c) Horizontal force coefficient, C_x, and vertical velocity component, v; (d) vertical force coefficient, C_y, and horizontal velocity component, u. Continuous lines indicate present results, while dashed lines indicate numerical results of [48].

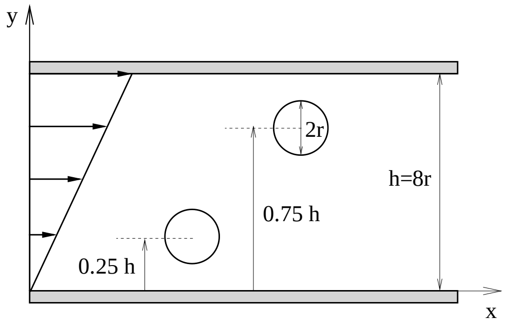

Figure 11: Sketch of the configuration for a circular particle transported in a shear flow between walls, at $Re_b = 40$.

obtained by [50]. Note that the migration velocity of the particles depends on the initial conditions at the early migration stage. Figure 12 reports the particle vertical position and migration velocity in function of time. With the prescribed initial slip velocity, the particle migrates gradually toward the equilibrium position, rotating with an instantaneous angular velocity that reaches an equilibrium value of about the 47% of the constant shear rate of the undisturbed flow field. This means that the particles rotate with the angular velocity of the flow field to within a small correction, as found also by Feng et al. [50].

3.4. Single sphere settling under gravity

To further validate the method, a three-dimensional case involving fluid-structure interaction with a rigid body is considered, by simulating the motion of a sphere falling under gravity in a closed container. Experimental investigations have been performed by [54], by means of particle image velocimetry, providing an accurate measure of both the sphere trajectory and velocity from the moment of its release until rest at the bottom of the channel. Given the relative small ratio between the box width and the particle diameter, the full flow field can be simulated under identical conditions. A sphere with diameter $d = 15\,mm$ is considered. The Froude and Reynolds numbers are defined as $Re = u_\infty d/\nu$ and $Fr = u_\infty/\sqrt{gd}$, where $g = 9.81\,m/s^2$ is the module of the gravity acceleration and u_∞ is the sedimentation velocity of a sphere in an infinite medium. In order to determine u_∞, the relation for the

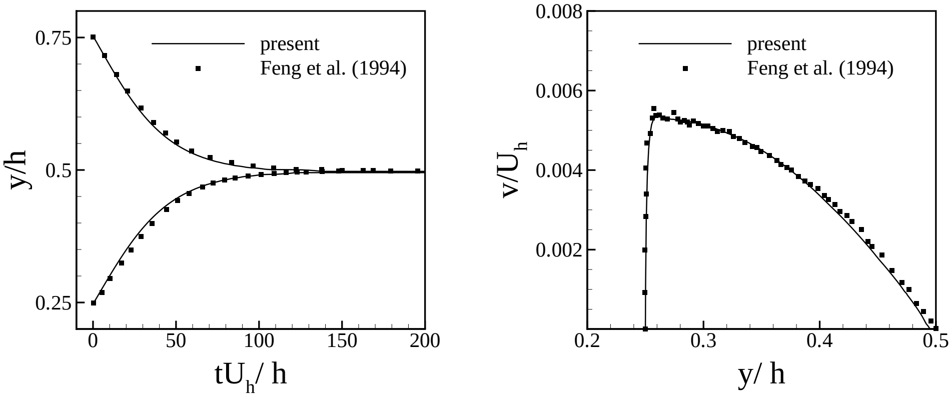

(a) (b)

Figure 12: Lateral migration of a circular neutrally buoyant particle in a shear flow between walls, at $Re_h = 40$. The particle is released at $y_0 = h/4$ and $y_0 = 3h/4$, with $\delta U_{init} = 0$. (a) Vertical baricentre position, y, versus time. (b) Migration vertical velocity, v, versus vertical baricentre position, y. Continuous lines indicate present results, symbols indicate numerical results of [50].

drag coefficient of Abraham [55] is used:

$$C_d = C_0 \left(1 + \frac{\delta_0}{\sqrt{Re}}\right)^2 \tag{49}$$

with $C_0\delta_0^2 = 24$ and $\delta_0 = 9.06$, obtaining

$$u_\infty = \sqrt{\frac{4gd}{3C_d}(\gamma - 1)} \tag{50}$$

Four different conditions are considered, with different density ratios, $\gamma = \rho_s/\rho_f$, and parameters, as reported in Table 1. The computational domain considered is $[0, 6.67d] \times [0, 6.67d] \times [0, 10.67d]$, where the last is the gravity acceleration direction. The particle starts falling with the centroid in $(3.33d, 3.33d, 8d)$. No-slip wall conditions are imposed at all the boundary surfaces of the domain. A uniform grid of $241 \times 241 \times 385$ nodes is used with a grid spacing of about $0.028d$. The Lagrangian markers are distributed uniformly onto the sphere surface, with a spacing of $0.02d$, that is equal to 0.71 the Eulerian grid size. The constant time step used depends on the case considered and is reported in Table 1. The sphere sedimentation velocity and trajectory are reported in Figure 13, where the present results are compared

Re_∞	γ	u_∞ (m/s)	Fr_∞	$\Delta t\, u_\infty/d$
1.5	1.155	0.038	0.0991	0.0001
4.1	1.161	0.060	0.156	0.0005
11.6	1.164	0.091	0.237	0.0007
31.2	1.167	0.128	0.334	0.001

Table 1: Reynolds number, density ratio, settling velocity in an infinite medium, Froude number and non-dimensional time step used in the simulation for the case of a sphere settling under gravity in a closed channel.

with the experimental data of [54]. A very good agreement is obtained for all the configurations considered.

3.5. Two-dimensional flexible filament in a free stream

A flexible filament motion in a free stream is simulated in order to test the ability of the simplified structural model to capture the dynamics of deformable bodies. Also in this case, a systematic verification study is performed to check the order of accuracy of the algorithm in the deformable-geometry case. The geometry of the problem is reported in figure 14. A zero-thickness filament of length L is pinned at the leading edge and freely moves under the effect of incoming flow and gravity. The initial orientation angle of the filament with respect to the flow is $\theta_0 = 0.1\pi$. The filament is considered inextensible ($k_e = 250000$) and flexible ($k_b = 0.15$) in order to replicate the test of [21] and [9]. The ratio of solid and fluid densities, γ is equal to 150. The Reynolds number, based on the filament length, L, the fluid density, ρ_f and the inflow velocity, U is equal to 200. The Froude number is equal to 0.5. The computational domain considered is $[-4L, 4L] \times [-2L, 6L]$ in the x and y directions respectively, with the filament leading edge in the origin of the domain and the gravity acting in the flow direction (negative y direction). No-slip wall boundary conditions are imposed at the vertical boundaries, while inlet and outlet boundary conditions are imposed at the horizontal ones, as indicated in figure 14. The filament has no thickness in the present simulation. Pressure and viscous forces acting on the filament are obtained considered two probes from each Lagrangian marker, in both directions, as explained in section 2.5. The mass of the nodes of the filament is calculated considering a thickness of $0.01L$. Seven non uniform

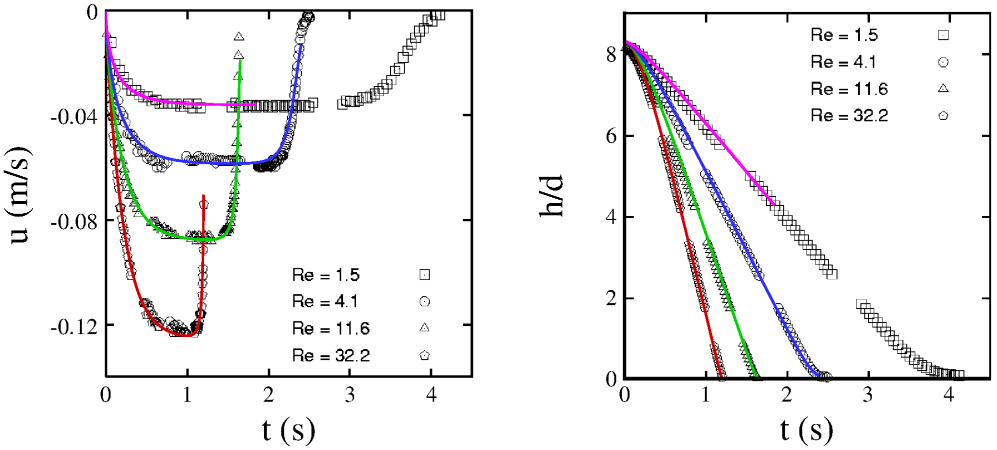

(a) (b)

Figure 13: Single sphere settling under gravity in a small container. (a) Spere sedimentation velocity; (b) sphere trajectory. Numerical results (continuous lines) are compared with experimental results (symbols) of ten Cate et al. [54] at four Reynolds numbers.

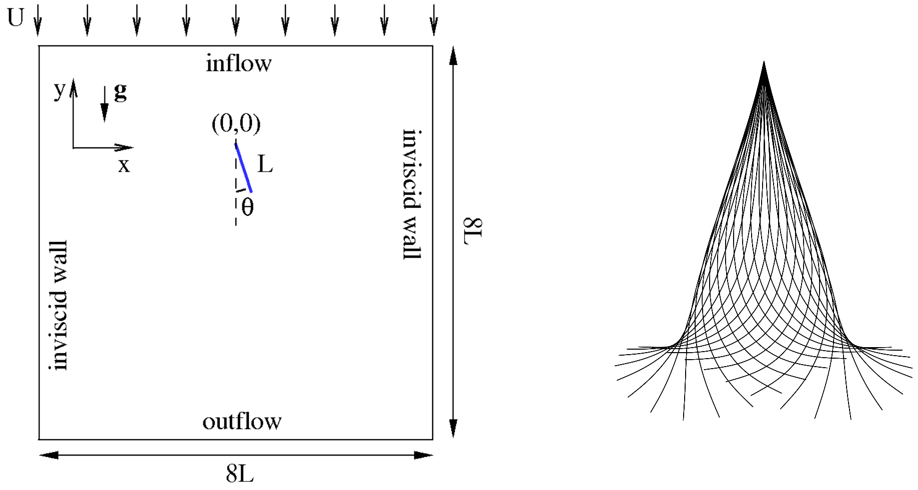

(a) (b)

Figure 14: (a) Scheme of the computational setup for the simulation of the flow around a flexible filament in a free stream. (b) Flapping filament configuration at several time points along its flapping cycle; $Re = 300$, $\gamma = 1$, $k_b = 0.1$.

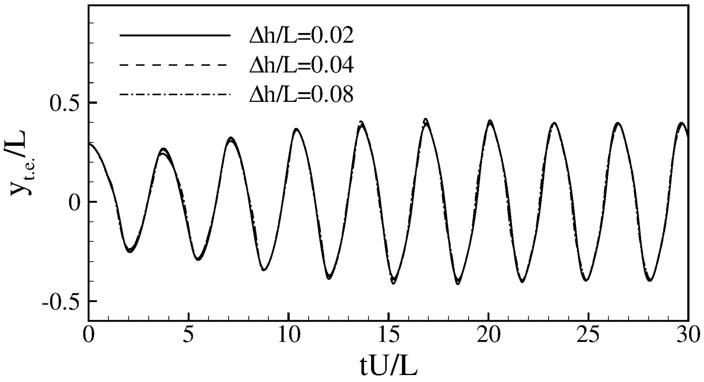

Figure 15: Comparison of trailing-edge transverse location time traces for a flexible filament in a free stream, with $Re = 200$, $\gamma = 150$ and $k_b = 0.15$.

Cartesian grids are used, refined in the vicinity of the filament, with nodes: 81×561, 101×701, 134×934, 161×1121, 201×1401, 267×1867, 401×2801, The grid spacing is maintained uniform in a box containing the filament of $[-1.2L, 1.2L] \times [-1L, 4L]$ in the x and y directions respectively, corresponding to an Eulerian grid spacing, $\Delta h/L$, of 0.05, 0.04, 0.03, 0.025, 0.02, 0.015, 0.01, respectively. A uniform Lagrangian marker spacing is adopted for all the cases, equal to 0.7 the Eulerian grid size. With the aim of investigating the overall numerical accuracy in both space and time, the time steps for each grid is chosen in order to mantain a constant ratio between the grid spacing and time step, $\Delta h/\Delta t = 10U_t$. The filament shows a periodic flapping state after few cycles. The filament configuration during the periodic flapping is reported in figure 14b for the finest case, showing the symmetric behavior of the structure deformation. In Figure 15 the present results in terms of time traces of the trailing edge transverse location of the flexible filament for the grids with local $\Delta h/L$ equal to 0.04, 0.02 and 0.01 are shown, showing very similar results, with some discrepancies of the coarse mesh with respect to the finer ones. For the accuracy study, the solution from the finest grid, 801×5601, is used as reference. Two relative errors are defined, for the maximum value of the filament trailing-edge transverse location, x_{max}, namely $\epsilon_A = (x_{max} - x_{max}^{ref})/x_{max}^{ref}$ and for the oscillation period, T, namely $\epsilon_T = (T - T^{ref})/T_{ref}$. The relative errors are reported versus grid spacing in Figure 16, showing an overall second-order accuracy on finer grids. The instantaneous vorticity contours at four time points along the flapping cycle

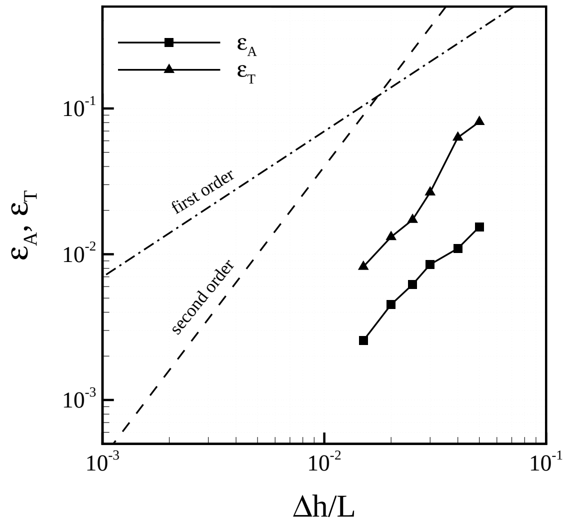

Figure 16: Systematic study of accuracy for a flexible filament in a free stream, with $Re = 200$, $\gamma = 150$ and $k_b = 0.15$.

are reported in figure 17. In Figures 18 and 19, the present results on the finest grid, in terms of time traces of the trailing-edge transverse location and drag and lift coefficients, respectively, are compared with numerical results of [21] and [9]. The results are in good agreement, with slight phase differences. The force coefficients are calculated by $C_F = 2F/\rho_f U^2 L$, where F is the hydrodynamic force acting on the filament in the streamwise (drag) and transverse (lift) directions, respectively. It is worth noting that no spurious oscillations are present even in the presence of deforming geometries for all the grids.

3.6. Three-dimensional flow around a flapping flag

As a three-dimensional test-case considering a deformable body, the flow around a flapping flag in a free stream is considered. The schematic of the problem is reported in figure 20, where a square flag of length L is considered. The computational domain is a rectangular box with $[-L, L] \times [-4L, 4L] \times [-L, 7L]$ in the x,y and z directions, respectively. The center of the leading edge of the flag is positioned at the origin. The initial shape of the flag is a flat plate, inclined of $\theta_0 = 0.1\pi$ with respect to the xz-plane, z being the streamwise direction and x the vertical one. The leading-edge of the

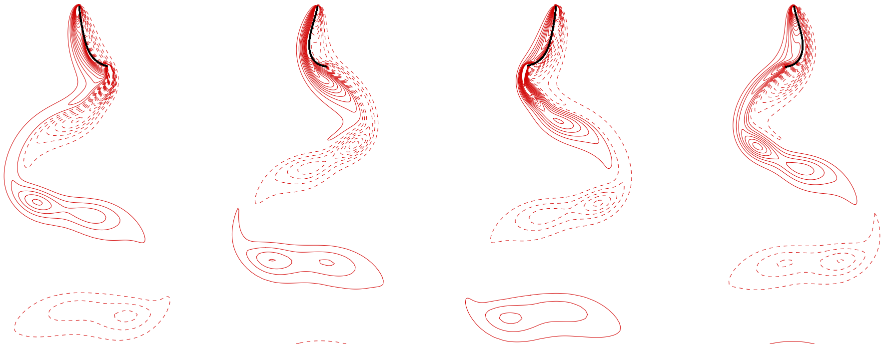

Figure 17: Instantaneous vorticity contours for the simulation of the flow around a flexible filament in a free stream, with $Re = 200$, $\gamma = 150$, $k_b = 0.15$. From left to right $t/T = 6$, $t/T = 6.25$, $t/T = 6.5$ and $t/T = 6.75$.

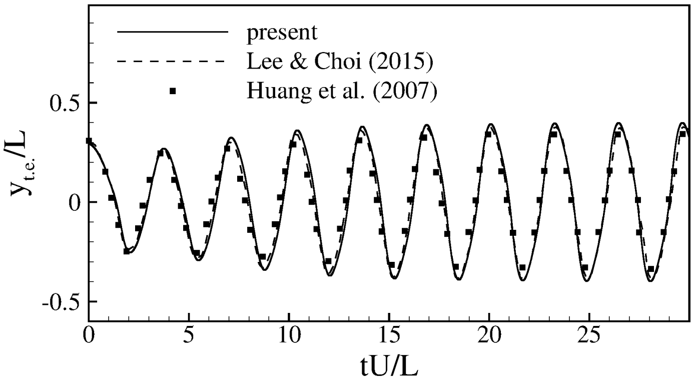

Figure 18: Comparison of trailing-edge transverse location time traces for a flexible filament in a free stream, with $Re = 200$, $\gamma = 150$ and $k_b = 0.15$. Present results (———), Lee and Choi [21] (– – –), Huang et al. [9] (■).

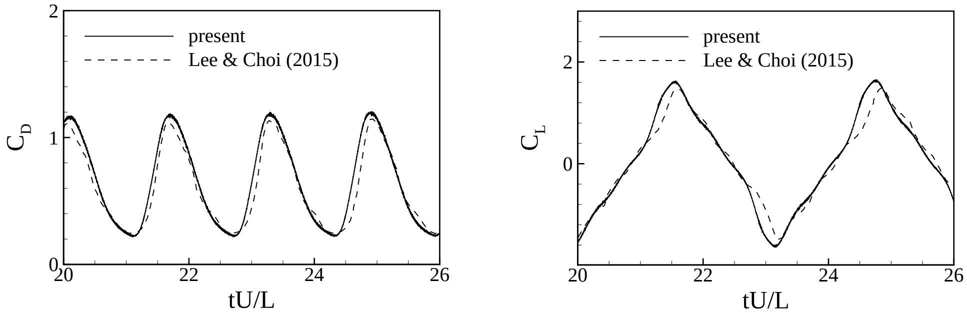

(a) (b)

Figure 19: Time histories of the drag (a) and lift (b) coefficients for a flexible filament in a free stream, with $Re = 200$, $\gamma = 150$ and $k_b = 0.15$. Present results (———), Lee and Choi [21] (– – –).

flag is pinned, while the other three edges are free to move. The simulation is performed on a nonuniform grid, refined around the flag and in the wake, with $101 \times 228 \times 260$, nodes and a uniform maximum resolution of $\Delta x = \Delta y = \Delta z = 0.02L$ near the flag. The flag is considered inextensible (the elastic constant is taken sufficiently large,$k_e = 2500$), and flexible ($k_b = 0.15$) in order to replicate the test of [9]. The ratio of solid and fluid densities, γ is equal to 100. The Reynolds number, based on L, the inflow velocity, U, and the fluid kinematic viscosity is equal to 200. No gravity is considered ($Fr = 0$). A constant time step is used of $\Delta t = 10^{-3}\, L/U$. Figure 21 shows the time traces of the middle point transverse location at the trailing edge of the flapping flag (filled circle in figure 20), compared with the numerical results of [20],[21] and [9]. A good agreement is obtained. The peak-to-peak excursion amplitude as well as the Strouhal number, defined as $St = fL/U$, for the middle trailing edge point, are reported in table 2, f being the oscillation frequency. Moreover, the time traces of force coefficients (drag and lift), obtained as $C_F = 2F/\rho_f U^2 L^2$, F being the hydrodynamic force in z (drag) or y (lift) direction, are shown in figure 22, compared with numerical results of [20] and [21]. The agreement is satisfactory. Finally, the instantaneous vortical structures, identified by Q-criterion [56] (iso-surface of $Q = 0.1$) around the flapping flag at $t/T = 2.41$ are reported in figure 23, showing the characteristic jairpin-like structure shed at each flapping [9].

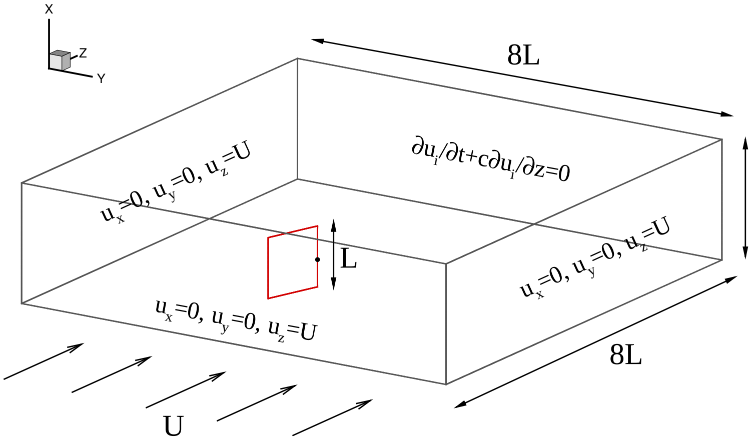

Figure 20: Problem description for the simulation of the flow arounf a flapping flag in a free stream.

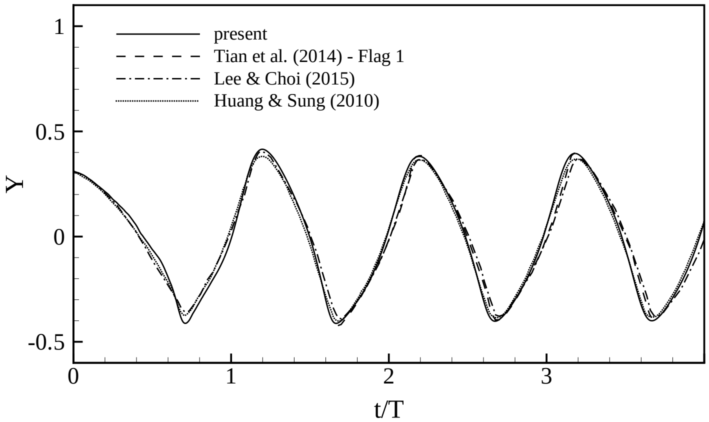

Figure 21: Time traces of the trailing-edge transverse location (middle point) of the flapping flag, for $Re = 200$, $Fr = 0$ and $\gamma = 100$.

	Amplitude A/L	Strouhal number St
present	0.795	0.265
Tian et al. (2014) - Flag 1	0.812	0.263
Lee & Choi (2015)	0.752	0.265
Huang & Sung (2010)	0.780	0.260

Table 2: Flapping flag in uniform flow with $Re = 200$, $Fr = 0$ and $\gamma = 100$. Comparison of peak-to-peak excursion amplitude, A/L, and the Strouhal number, St, for the middle trailing-edge point.

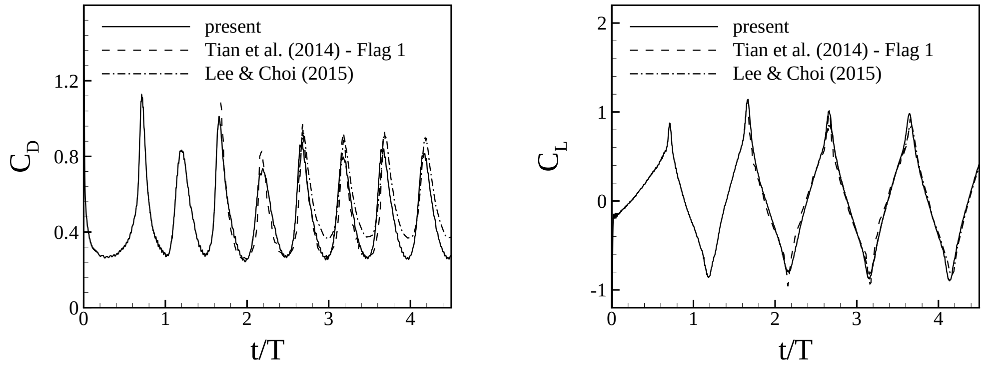

Figure 22: Time traces of the drag and lift coefficients of the flapping flag, for $Re = 200$, $Fr = 0$ and $\gamma = 100$.

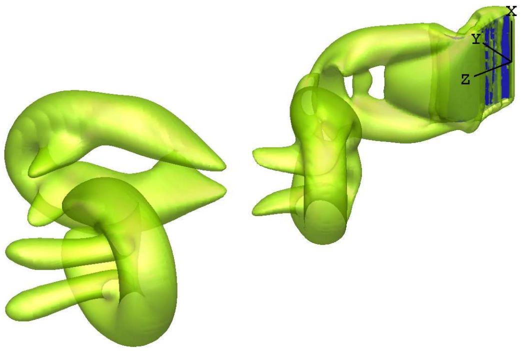

Figure 23: Vortical structures (q-criterion) around the flapping filament at $t/T = 2.41$, for $Re = 200$, $Fr = 0$ and $\gamma = 100$.

3.7. Three-dimensional inverted flag in a free stream

The dynamics of an inverted flag is considered in order to test the simplified structural model in the case of very large deformation and to test the sensitivity of the model to the bending stiffness parameter. With the aim of harvesting fluid kinetic energy, flow-induced flapping of an elastic sheet has recently been proposed. However, an efficient system for energy harvesting has to easily become unstable, even at low velocities, and have high excitation amplitude [57]. The configuration adopted is that of an inverted filament, with a free leading edge and a clamped trailing edge. Experimental investigations by [57] on the flapping dynamics of an inverted elastic sheet, have shown that the sheet response can be largely divided in three modes, depending on the bending stiffness of the plate. A straight mode is observed for high bending, with the sheet that remains straight or flutters with very small amplitudes around the equilibrium position; a periodic flapping from side to side, with large amplitudes is found for intermediate bending; another quasi-steady behavior is observed for low bending, with the sheet that bends in one direction and maintains a highly curved shape, fluttering with small amplitudes around this deflected configuration. The proposed method is therefore used to capture the different dynamics varying the bending coefficient of the network-spring model. The schematic of the problem is the same used in the flapping flag case 20, where a square flag of length L is considered in a computational domain with size $[-L, L] \times [-4L, 4L] \times [-L, 7L]$ in the x,y and z directions, respectively, with the center of the leading edge of the flag positioned at the origin. The initial shape of the flag is a flat plate, with no inclination with respect to the xz-plane, z being the streamwise direction and x the vertical one. The trailing-edge of the flag is clamped, while the other three edges are free to move. No gravity is considered. The simulation is performed on a nonuniform grid, refined around the flag and in the wake, with $101 \times 228 \times 260$, nodes and a uniform maximum resolution of $\Delta x = \Delta y = \Delta z = 0.02L$ near the flag. In order to compare the results with the experiments of [57], two non-dimensional dynamical parameters are considered, the bending-stiffness, β, and the mass ratio, γ, here defined as:

$$\beta = \frac{B}{\rho_f U^2 L^3} \quad \text{and} \quad \gamma = \frac{\rho_s h}{\rho_f L}\,, \tag{51}$$

where B is the flexural rigidity of the sheet, ρ_f and ρ_s are the fluid and sheet densities, respectively, U is the undisturbed flow velocity and h is the

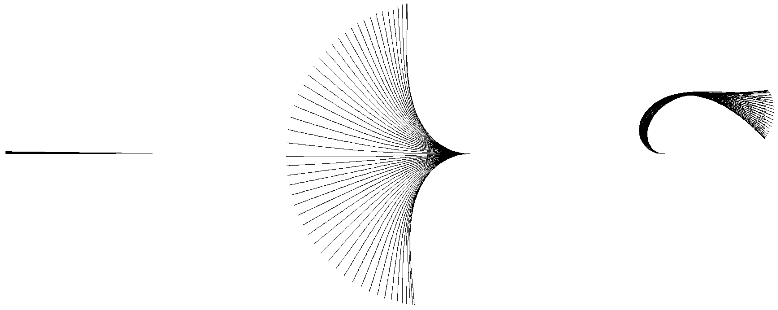

Figure 24: Inverted flexible filament in a free stream at $Re = 200$, $\gamma = 1$. From left to right, the bending rigidity decreases, showing a *straight mode* (left), a *flapping mode* (middle) and a *deflected mode* (right). No gravity is considered.

sheet thickness. The flag is considered inextensible (the elastic constant is taken sufficiently large,$k_e = 5000$), while the bending constant is calculated by equation **??**, assuming different values to replicate the abovementioned three different behaviors. The Reynolds number, based on L, the inflow velocity, U, and the fluid kinematic viscosity, ν is considered equal to 200 (lower than that in the experiments of [57]. A constant time step is used of $\Delta t = 10^{-3}\, L/U$.

Figure 24 reports the superimposed filament positions in time, showing straight, flapping and deflected modes, respectively, as the bending rigidity of the model is reduced. Additionally, the free leading edge vertical position in time is shown in figure 25, with a clear periodic behavior for the flapping mode and a more complex reduced fluttering with a non clear periodicity for the deflected mode and (with smaller amplitude) straight mode. Finally, the free leading edge vertical position in time for the case with $Re = 250$, $\gamma = 2$, $k_b = 20$, is compared with the corresponding experimental results of [57] with a bending stiffness parameter β equal to 0.1. A very good agreement is obtained also in this test.

3.8. Three-dimensional flow through a bio-prosthetic aortic valve

Finally, a three-dimensional test case is presented in order to test the thin-structure dynamics under high pressure gradients. The case considered is that of a bioprosthetic aortic valve, with three deformable cusps that open and close under a pulsatile flowrate. The flow domain considered reproduces the initial tract of the ascending aorta, with a geometry similar to that used

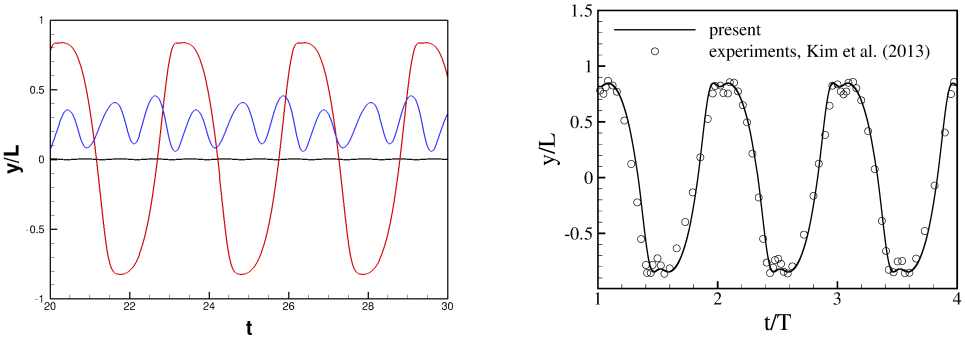

Figure 25: Left: inverted flexible filament in a free stream at $Re = 200$, $\gamma = 1$. Time history of the y-coordinate of the tip. Right: comparison of the y-coordinate of the filament tip for the case with $Re = 250$, $\gamma = 2$, $k_b = 20$; symbols indicate experimental results of [57] with $\beta = 0.1$.

in [58]. It is considered rigid and composed of i) an inflow circular tube upstream of the valve, with the same diameter of the valve and length h_1; ii) a tract with three sinuses of Valsalva reproducing the physiological case, with length h_s; iii) a larger tube after the sinuses, with larger diameter, D, and length h_3. All the geometrical parameters are given in figure 26a, along with a schematic of the problem. The valve considered wants to mimic the Trifecta valve model (St Jude Medical Inc., Minneapolis), which is a trileaflet tissue valve constructed using a polyester and tissue-covered titanium stent. The leaflets are made of pericardial tissue and are attached to the exterior of the stent in order to mimic the hemodynamics performance of a healthy aortic heart valve. The valve has a diameter $d_0 = 23mm$, and height h_l, as shown in figure 26a. The leaflet geometry is obtained reproducing the real valve stress-free geometry, as reported in figure 26b. The leaflets nodes corresponding to the stent position (thick black lines in figure 26b) are constrained to be fixed in time. Moreover, a geometrical constraint is adopted considering three vertical planes at 120° and passing through the center of the orifice, allowing only sliding of the structural nodes on the planes and preventing the leaflets from passing through each other. It is worth noting that contact between two nodes of different structures could be easily modeled using properly defined interaction potentials and adding a repulsion force to the total forces acting on a single node, but here a geometrical approach has been adopted for simplicity. The elastic behavior of the pericardial tissue is modeled with the simplified, nonlinear anisotropic model described in section 2.4. Bending

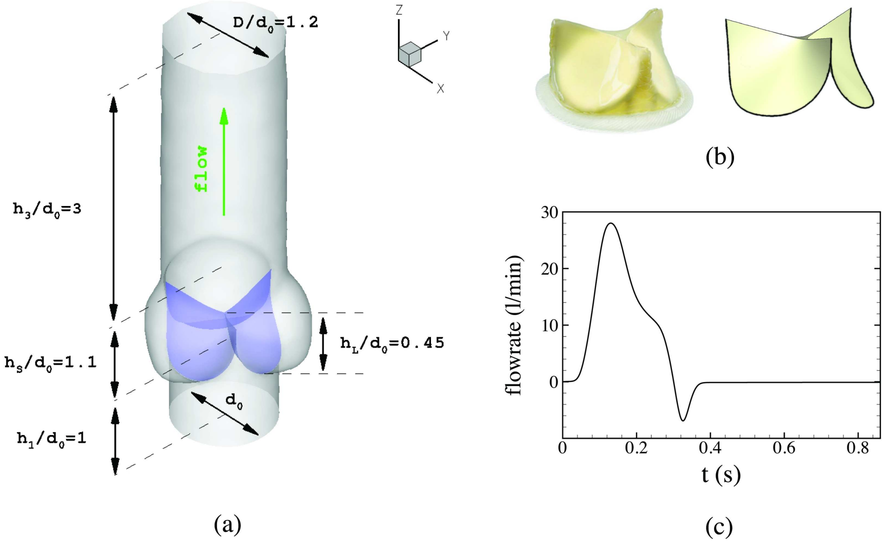

(a)

(b)

(c)

Figure 26: (a) Scheme of the consiguration for the three-dimensional flow through a bioprosthetic aortic valve. The main geometrical parameters are shown, related to the valve diameter, $d_0 = 23\,mm$. (b) Trifecta aortic valve real model (St Jude Medical Inc., Minneapolis) and stress-free computational model (on the left) of the three leaflets. Thick black lines indicate the constrained edges. (c) Pulstile flowrate adopted in the simulations.

stiffness is also added to the model, using a bending constant $k_b = 0.01$. The material density is set equal to that of the fluid and a constant thickness of $0.5\,mm$ is considered. A nonuniform grid with $257 \times 257 \times 372$ nodes is used in x,y and z directions, respectively, z being the streamwise direction, with an Eulerian grid spacing near the valve $0.01d_0$, and an averaged Lagrangian marker spacing of $0.007d_0$ on the leaflets. A constant CFL value of 0.25 is adopted, leading to a variable temporal resolution ranging from 200 to $2\mu s$ during the simulation. A pulsatile flowrate is imposed in the inlet section of the domain, with a cardiac output of approximately $5l/min$, at a fixed beat rate of $70 beats/min$ (see figure 26c), while standard convective outflow conditions are imposed at the outlet section. The blood density is set to $1060kg/m^3$. The peak Reynolds number is about 6700, based on the inlet velocity, the inflow tube diameter and the blood kinematic viscosity.

Figure 27 shows a comparison between the real valve in in-vitro experiments (St. Jude Medical Inc., www.sjm.com) and the present numerical results, at two different time instants during the opening phase, indicated with open circles in figure 28a. Moreover, the comparison of numerical and experimental projected valve area (PVA) seen from the top of the domain in the xy plane, divided by its maximum value assumed during the cardiac cycle, PVA_{max}, is shwon in figure 28a. The agreement with experiments of the valve leaflets dynamics and projected area is very good, considering the complexity of the model and the uncertainty in the material properties. Furthermore, it is important to stress that experimental data are obtained by valve visualization from the valve manufacturer website, with no information about the exact flowrate waveform. Figure 28b reports one leaflet configuration at some instants during the cycle indicated by symbols in figure 28a. Finally, the valve configuration and the streamwise velocity contours, along with the instantaneous vortical structures, identified by Q-criterion [56] (iso-surface of $Q = 0.1$), at three different instants of the cardiac cycle are reported in figures 29-31. The jet-like flow that emerges from the central orifice of the valve is clearly shown, with high shear stresses occurring at the edge of the jet during the deceleration phase. Large-scale vortical structures form, starting from the leaflet commissures and in the three sinuses of Valsalve during the acceleration phase. After peak systole, instabilities occur at the edge of the jet and smaller scale structures are developed, still maintaining a clear central jet, as shown in figure 30. The flow appears more disordered during the deceleration phase at late systole, with decreasing flowrate and small scale vortical structures that fill completely the domain. It is impor-

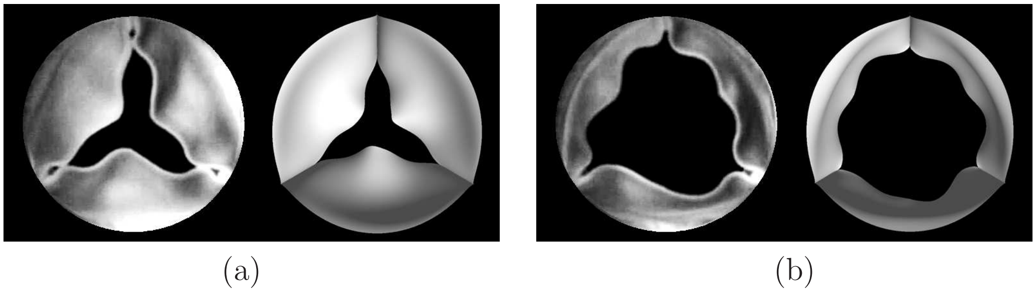

Figure 27: Instantaneous snapshots of the valve leaflets dynamics from an experimental visualization (on the left of each figure) and numerical results (on the right of each figure), at two instants during the opening phase, indicated with open circles in figure 28a.

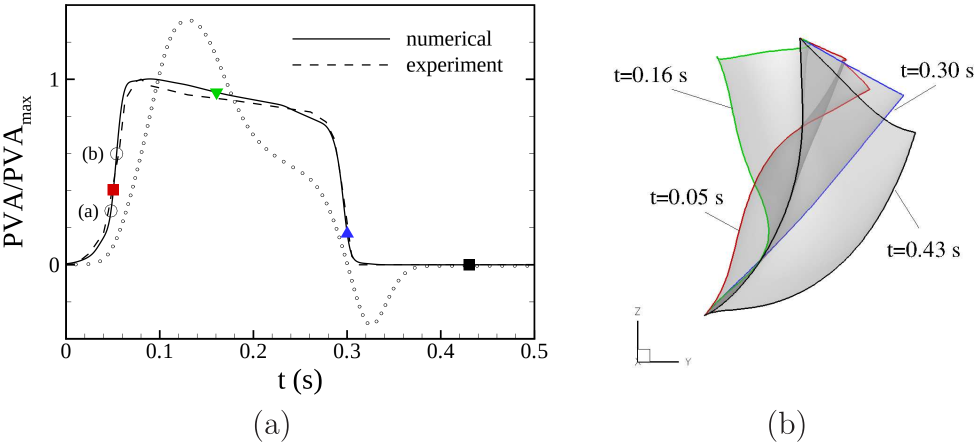

Figure 28: (a) Projected valve area PVA divided by its maximum value assumed on the cycle, PVA_{max} for a cardiac cycle for numerical simulations (continuous line) and experiments (dashed lines). (b) Leaflet configuration at some instants during the cycle indicated by symbols in figure 28a.

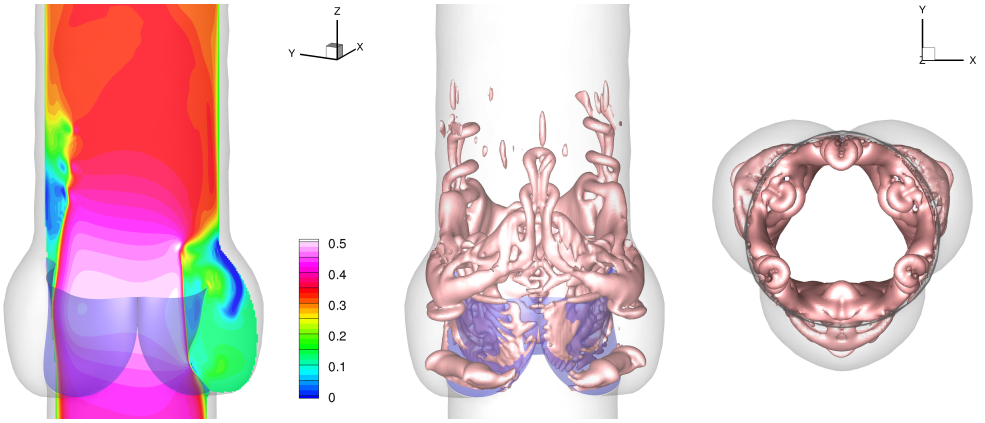

Figure 29: Peak of flowrate ($t = 0.13\,s$). Left: streamwise velocity contours (in m/s) in the yz plane. Right: instantaneous vortical structures identified by Q-criterion (isosurfaces of $Q = 0.1$).

tant to note that the structural model performance are promising and the valve dynamics is reasonably accurate, with a very reduced computational cost (about 1%) with respect to the fluid solver one.

4. Conclusions

A versatile numerical method for the fluid-structure-interaction of bodies of arbitrary thickness, immersed in an incompressible fluid, is presented, with the aim of simulating different biological engineering applications. A partitioned, discrete-forcing immersed boundary method is adopted, based on a moving least squares method to reconstruct the solution in the vicinity of the immersed surface and to convert the Lagrangian forcing back to the Eulerian grid. A simple spring-network model is considered for describing the dynamics of non-rigid bodies and structures, in order to have the freedom of easily model and simulate different biological systems that can not always be described by simple continuum models, without affecting the computational time and simplicity of the overall method. The surfaces can be rigid or deformable, and can be either closed, in order to describe solid bodies or capsules and biological cells, or open, describing slender bodies, such as filaments or organ tissues. Fluid and structures are coupled in a strong way, in order to avoid instabilities related to large accelerations due to the deformations of the surfaces. The evaluation of the hydrodynamic

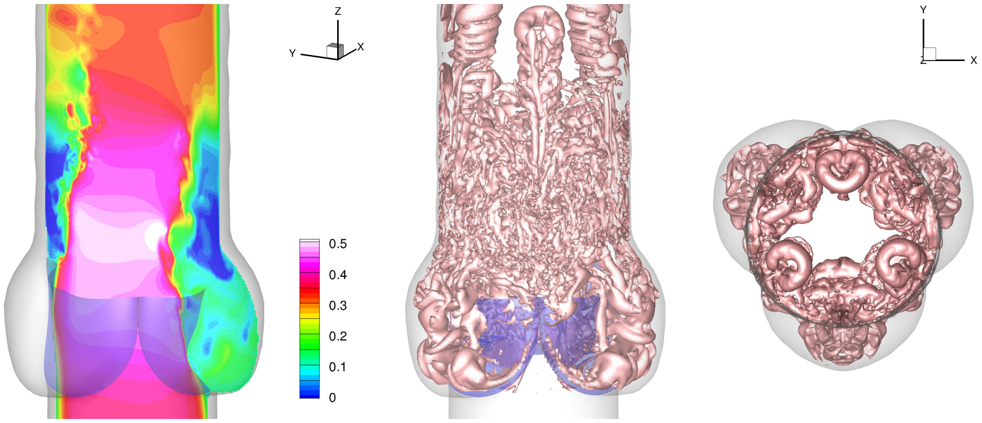

Figure 30: Early systole ($t = 0.16\,s$). Left: streamwise velocity contours (in m/s) in the yz plane. Right: instantaneous vortical structures identified by Q-criterion (isosurfaces of $Q = 0.1$).

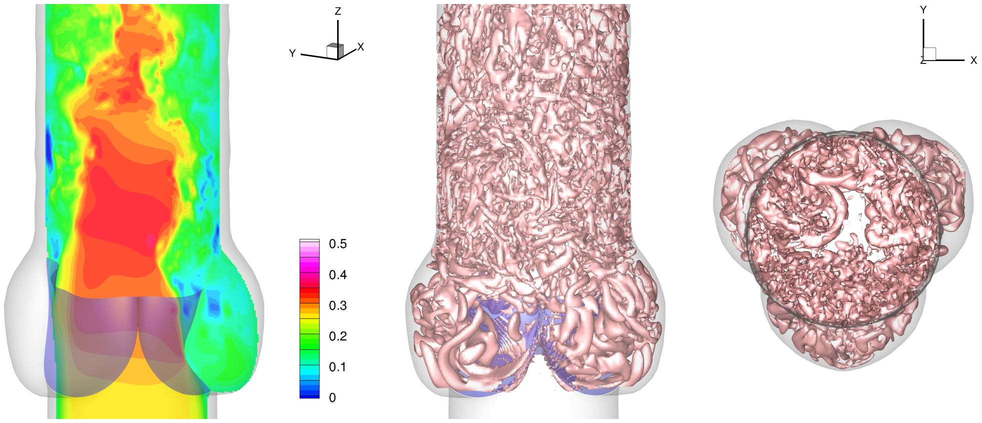

Figure 31: Late systole ($t = 0.23\,s$). Left: streamwise velocity contours (in m/s) in the yz plane. Right: instantaneous vortical structures identified by Q-criterion (isosurfaces of $Q = 0.1$).

loadings on the structure requires particular attention, in particular of the case of structures of zero-thickness. In this case, two probes are sent from each location at which the forces need to be calculated, along both sides of the normal-to-surface direction, evaluating the pressure and velocity gradient near the body. The method gives accurate results comparable with that of sharp direct-forcing approach, and can manage pressure differences across the surface in one grid cell, still obtaining very smooth forces. The immersed boundary technique as well as the structural solver do not impose any restriction to the computational time step, which is determined based on stability conditions of the flow solver. The accuracy of the method has been validated by means of several test cases of increasing complexity. Several testcases with rigid bodies falling in a quiescent fluid, fluttering or tumbling, or transported by a shear flow are presented, showing a very good agreement with available experimental data and numerical results obtained by different approaches. In the abovementioned cases, the surface is closed and undeformable, enclosing a volume and thus representing a rigid particle. Then, open surfaces representing infinitely thin elastic structures with mass are considered: a two-dimensional flexible filament and an inverted flexible filament in a free stream. A very good agreement has been obtained in all the cases, as shown by comparison with numerical and experimental results available in the literature. Therefore, in all the test considered, the method proves to be accurate and efficient in handling both rigid and deformable bodies, even using a simplified description of the mechanical properties of the structure. Finally, a three-dimensional model of a bio-prosthetic aortic valve is considered, with nonlinear and anisotropic mechanical properties, opening and closing during a pulsatile cardiac cycle, showing a good qualitative agreement with respect to in-vitro data, considering the complexity of both the geometry and the material properties of the biological tissue.

References

[1] B.S.H. Connell and D.K.P. Yue. Flapping dynamics of a flag in a uniform stream. *Journal of Fluid Mechanics*, 581:33–67, 2007.

[2] T. Sawada and T. Hisada. Fluid-structure interaction analysis of the two-dimensional flag-in-wind problem by an interface-tracking ALE finite element method. *Computers & Fluids*, 36:136–146, 2007.

[3] C. S. Peskin. Flow patterns around heart valves: A numerical method. *J. Comput. Phys.*, 10:252, 1972.

[4] R. Mittal and G. Iaccarino. Immersed boundary methods. *Annu. Rev. Fluid Mech.*, 37:239, 2005.

[5] L.J. Fauci and C.S. Peskin. A computational model of aquatic animal locomotion. *Journal of Computational Physics*, 77:85–108, 1988.

[6] L. Zhu and C.S. Peskin. Simulation of a flapping flexible filament in a flowing soap film by the immersed boundary method. *Journal of Computational Physics*, 179:452–468, 2002.

[7] Y. Kim and C.S. Peskin. Penalty immersed boundary method for an elastic boundary with mass. *Physics of Fluids*, 19:053103, 2007.

[8] Y. Kim and M.C. Lai. Simulating the dynamics of inextensible vesicles by the penalty immersed boundary method. *Journal of Computational Physics*, 229:4840–4853, 2010.

[9] W. Huang, S.J. Shin, and Sung H.J. Simulation of flexible filaments in a uniform flow by the immersed boundary method. *Journal of Computational Physics*, 226:2206–2228, 2007.

[10] D. Goldstein, R. Handler, and L. Sirovich. Modeling no-slip flow boundary with an external force field. *J. Comput. Phys.*, 105:354–366, 1993.

[11] E. A. Fadlun, R. Verzicco, P. Orlandi, and J. Mohd-Yosuf. Combined immersed-boundary finite-difference methods for three-dimensional complex flow simulations. *J. Comput. Phys.*, 161:35, 2000.

[12] Kim J., Kim D., and Choi H. An immersed-boundary finite volume method for simulations of flow in complex geometries. *J. Comput. Phys.*, 171:132–150, 2001.

[13] M. Uhlmann. An immersed boundary method with direct forcing for the simulation of particulate flows. *Journal of Computational Physics*, 209:448–476, 2005.

[14] J. Yang and E. Balaras. An embeeded-boundary formulation for large-eddy simulation of turbulent flows interacting with moving boundaries. *Journal of Computational Physics*, 215:12–40, 2006.

[15] M. Vanella and E. Balaras. A moving-least-squares reconstruction for embedded-boundary formulations. *Journal of Computational Physics*, 228:6617–6628, 2009.

[16] J. Lee, J. Kim, and H. Choi. Sources of spurious force oscillations from an immersed boundary method for moving-body problems. *Journal of Computational Physics*, 230:2677–2695, 2011.

[17] J.H. Seo and R. Mittal. A sharp-interface immersed boundary method with improved mass conservation and reduced spurious pressure oscillations. *Journal of Computational Physics*, 230:7347–7363, 2011.

[18] H. Luo, R. Mittal, X. Zheng, S.A. Bielamowicz, R.J. Walsh, and J.K. Hahn. An immersed-boundary method for flowstructure interaction in biological systems with application to phonation. *Journal of Computational Physics*, 227:9303–9332, 2008.

[19] B. Yin and H. Luo. Effect of wing inertia on hovering performance of flexible flapping wings. *Physics of Fluids*, 22:111902, 2010.

[20] F.B. Tian, H. Dai, H. Luo, F.J. Doyle, and B. Rousseau. Fluid-structure interaction involving large deformations: 3d simulations and applications to biological systems. *Journal of Computational Physics*, 258:451469, 2014.

[21] I. Lee and H. Choi. A discrete–forcing immersed boundary method for the fluid–structure interaction of an elastic slender body. *Journal of Computational Physics*, 280:529–546, 2015.

[22] A. Gilmanov, T.B. Le, and F. Sotiropoulos. A numerical approach for simulating fluid structure interaction of flexible thin shells undergoing arbitrarily large deformations in complex domains. *Journal of Computational Physics*, 300:814–843, 2015.

[23] C. Pozrikidis. *Computational Hydrodynamics of Capsules and Biological Cells*. Chapman & Hall / CRC Press, 2010.

[24] D. Barthes-Biesel. Modeling the motion of capsules in flow. *Current Opinion in Colloid & Interface Science*, 16:3–12, 2011.

[25] M. Tanaka, S. Wada, and M. Nakamura. *Computational biomechanics*. Springer, 2012.

[26] R.W. Hammings. Stable predictor–corrector methods for ordinary differential equations. *Journal of the ACM*, 6:37–47, 1959.

[27] R.L. Taylor, E. Onate, and P.A. Ubach. Finite element analysis of membrane structures. *Textile Composites and Inflatable Structures*, 3:47–68, 2005.

[28] P. Orlandi. *Fluid flow phenomena: a numerical toolkit*. Kluwer Academic Publishers, 2000.

[29] R. Verzicco and P. Orlandi. A finite difference scheme for three-dimensional incompressible flows in cylindrical coordinates. *Journal of Computational Physics*, 123:402–413, 1996.

[30] N. Swartzrauber, P. A direct method for the discrete solution of separable elliptic equations. *SIAM J. Numer. Anal.*, 11:11361150, 1974.

[31] G. Liu and Y.T. Gu. *An Introduction to Meshfree Methods and their Programming*. Springer, 2005.

[32] A. Van Gelder. Approximate simulation of elastic membranes by triangulated spring meshes. *Journal of Graphics Tools*, 3:21–42, 1998.

[33] Y. Kantor and D.R. Nelson. Phase transitions in flexible plymeric surfaces. *Physical Review A*, 36:4020–4032, 1987.

[34] J. Li, M. Dao, C.T. Lim, and S. Suresh. Spectrin-level modeling of the cytoskeleton and optical tweezers stretching of the erythrocyte. *Biophysical Journal*, 88:3707–3719, 2005.

[35] D.A. Fedosov, Caswell B., and G.E. Karniadakis. Systematic coarse-graining of spectrin-level red blood cell models. *Computer Methods in Applied Mechanics and Engineering*, 199:1937–1948, 2010.

[36] H. Delingette. Triangular springs for modeling nonlinear membranes. *IEEE Transactions on visualization and computer graphics*, 14:329–341, 2008.

[37] M. Chen and F.J. Boyle. Investigation of membrane mechanics using spring networks: Application to red-blood-cell modelling. *Materials Science and Engineering C*, 43:506–516, 2014.

[38] J.C. Hansen, R. Skalak, S. Chien, and A. Hoger. An elastic network model based on the structure of the red blood cell membrane skeleton. *Biophysical Journal*, 70:146–166, 1996.

[39] D.E. Discher, D.H. Boal, and S.K. Boey. Simulations of the erythrocyte cytoskeleton at large deformation. II. Micropipette aspiration. *Biophysical Journal*, 75:1584–1597, 1998.

[40] M.M. Dupin, I. Halliday, C.M. Care, and L.L. Munn. Lattice Boltzmann modelling of blood cell dynamics. *International Journal of Computational Fluid Dynamics*, 22:481–492, 2008.

[41] H.M. Ezzeldin, M.D. de Tullio, M. Vanella, S.D. Solares, and E. Balaras. A strain-based model for mechanical hemolysis based on a coarse-grained red blood cell model. *Annals of Biomedical Engineering*, 43:1398–1409, 2015.

[42] M. Thubrikar. *The aortic valve.* CRC Press, Boca Raton, FL, USA, 1990.

[43] P. Hammer, M. Sacks, P. del Nido, and R. Howe. Mass-spring model for simulation of heart valve tissue mechanical behavior. *Annals of Biomedical Engineering*, 39:1–12, 2011.

[44] Y.C. Fung. *Biodynamics. Circulation.* Springer-Verlag, New York Berlin Heidelberg Tokyo, 1984.

[45] M. D. de Tullio, A. Cristallo, E. Balaras, and R. Verzicco. Direct numerical simulation of the pulsatile flow through an aortic bileaflet mechanical heart valve. *Journal of Fluid Mechanics*, 622:259–290, 2009.

[46] Z. Xia, K.W. Connington, S. Rapaka, P. Yue, Feng J.J., and S. Chen. Flow patterns in the dedimentation of an elliptical particle. *Journal of Fluid Mechanics*, 625:249–272, 2009.

[47] A. Belmonte, H. Elsenberg, and E. Moses. From flutter to tumble: Inertial drag and Froude similarity in falling paper. *Physical Review Letters*, 81:345–348, 1998.

[48] H. Hui Wan, H. Dong, and Liang Z. Vortex formation of freely falling plates. In *50th AIAA Aerospace Sciences Meeting including the New Horizons Forum and Aerospace Exposition*. Tennessee, Jan. 9-12, 2012.

[49] J. Feng, H.H. Hu, and D.D. Joseph. Direct simulation of initial value problem for the motion of solid bodies in a Newtonian fluid. Part 1. sedimentation. *Journal of Fluid Mechanics*, 261:95, 1994.

[50] J. Feng, H.H. Hu, and D.D. Joseph. Direct simulation of initial value problem for the motion of solid bodies in a Newtonian fluid. Part 2. Couette and Poiseuille flows. *Journal of Fluid Mechanics*, 277:271–301, 1994.

[51] B.P. Ho and G. Leal. Inertial migration of rigid spheres in two-dimensional unidirectional flows. *Journal of Fluid Mechanics*, 65:365–400, 1974.

[52] P. Vasseur and R.G. Cox. The lateral migration of a spherical particle in two-dimensional shear flows. *Journal of Fluid Mechanics*, 78:385–413, 1976.

[53] J.S. Halow and G.B. Wills. Experimental observations of sphere migration in Couette systems. *Industrial & Engineering Chemistry Fundamentals*, 9:603, 1970.

[54] A. ten Cate, C.H. Nieuwstad, J.J. Derksen, and Van den Akker H.E.A. Particle imaging velocimetry experiments and lattice-Boltzmann simulations on a single sphere settling under gravity. *Physics of Fluids*, 14:4012–4025, 2002.

[55] F. Abraham. Functional dependence of drag coefficient of a sphere on Reynolds number. *Physics of Fluids*, 13:2194, 1970.

[56] J.C. Hunt, A. Wray, and P. Moin. Eddies, stream, and convergence zones in turbulent flows. *Center for Turbulence Research Report*, CTR-S88, 1988.

[57] D. Kim, J. Cosse, C.H. Cerdeira, and M. Gharib. Flapping dynamics of an inverted flag. *Journal of Fluid Mechanics*, 736:R1, 2013.

[58] M. D. de Tullio, G. Pedrizzetti, and R. Verzicco. On the effect of aortic root geometry on the coronary entry-flow after a bi-leaflet mechanical heart valve implant: A numerical study. *Acta Mechanica*, 216:147–163, 2011.